Joining of additively manufactured fiber-reinforced thermoplastic and metals by ultrasonic energy: Mechanical and corrosion behavior

Willian S. de Carvalho [a],[*], Guilherme S. Vacchi [b], Carlos A.D. Rovere [b], Sergio T. Amancio-Filho [a],[*]

[a] Graz University of Technology – TU Graz, Institute of Materials Science, Joining and Forming, BMK Endowed Professorship for Aviation, Kopernikusgasse 24/1, 8010 Graz – Austria

[b] Federal University of São Carlos – UFSCar, Department of Materials Engineering, Rodovia Washington Luis Km 235, 13565-905 São Carlos, SP, Brazil

ARTICLE INFO

ABSTRACT

Ultrasonic joining (U-Joining) is applied to create reinforced hybrid joints between unreinforced or fiber-reinforced polymers and surface-structured metals. While the feasibility of joining additively manufactured (AM) materials was already demonstrated, a detailed description of the process parameters' effects is still missing. Therefore, this study aims to define the influence of the U-Joining parameters on the mechanical and corrosion properties of AM 20% short-carbon-fiber-reinforced poly-ether-ether-ketone (PEEK-20CF) and 316L stainless steel (316L SS) hybrid joints. Optimal joining parameters were determined via Box-Behnken design of experiments to maximize the joints' ultimate lap shear forces (ULSF) and displacement at break (DaB), where the results increased from 1.4 ± 0.2 kN to 3.6 ± 0.3 kN (2.6 times) and from 1.2 ± 0.3 mm to 2.4 ± 0.1 mm (2 times), respectively. Microstructural analyses revealed a strong micromechanical interlocking between the parts due to the filling of crevices at the as-built AM metallic part's rough surface by consolidated PEEK-20CF, which resulted in a mixture of adhesive, cohesive and net tension failure during the lap-shear tests. Finally, the corrosion resistance was also evaluated by potentiodynamic polarization curves, showing that the energy input during the joining cycle slightly reduced the pitting corrosion resistance of the 316L part.

1. Introduction

The transportation industries have extensively researched lightweight structures to reduce greenhouse gas emissions and meet strict environmental regulations [1,2]. Original equipment manufacturers (OEMs) are successfully integrating carbon fiber-reinforced polymers (CFRP) and metallic alloys to create lightweight hybrid structures that can improve their vehicles' energy efficiency [3]. This key approach has been demonstrated in successful examples such as the Boeing 787 Dreamliner and the Airbus A350 XWB, which incorporate around 50% and 53% of CFRP, respectively, in their structures alongside other metallic alloys [4,5].

The production of metal-fiber reinforced polymer hybrid structures is a challenging task, mainly due to the physical and chemical differences involved, resulting in poor compatibility and distortion of parts when thermally joined [6]. Therefore, metal-fiber reinforced polymer joints are usually the most susceptible to failure during service in hybrid structures. Various methods have been suggested to address these issues,

but a single joining solution capable of overcoming all the challenges is still unavailable. The two most frequently used methods for joining are adhesive bonding and mechanical fastening, but each has its own limitations and disadvantages. Adhesive bonding tends to be brittle and has poor out-of-plane strength [7,8], requiring surface preparation and specific fixtures [9]. Mechanical fastening, on the other hand, relies on the use of third-party materials like screws, rivets, or bolts and requires pre-hole drilling, leading to stress concentration, corrosion issues, and fatigue cracking [10,11]. Additionally, both methods add extra weight to the structure, which hinders the capacity of metal-fiber reinforced polymer hybrid structures to reduce weight.

Recent research suggests that incorporating through-the-thickness reinforcements (TTRs) on the metal surface can enhance the mechanical performance of metal-fiber reinforced polymer hybrid joints [12,13]. Such novel concepts are currently known as direct assembly (DA) [11]. They initially consist of the metal surface structuring via a subtractive [14], additive [15,16] or formative process [17]. Secondly, a thermoplastic or thermoset-based composite is mounted onto the structured

* Corresponding authors.
E-mail addresses: willian.salesdecarvalho@student.tugraz.at (W.S. de Carvalho), sergio.amancio@tugraz.at (S.T. Amancio-Filho).

metallic surface, creating hybrid joints or structures with enhanced out-of-plane strength [18–21]. Despite these benefits, DA processes have primarily been used for metal-thermoset composite parts that have long curing cycles and limited recyclability, making it difficult to meet the demands of a circular economy [15]. These limitations result in an open niche for new joining and DA technologies that combine the improvements resulting from TTRs and faster-assembling cycles.

The development of the ultrasonic joining (U-Joining) process aimed to address these challenges, allowing the assembling of unreinforced and fiber-reinforced thermoplastics and surface-structured metallic parts [22]. This technology has the advantage of reducing assembly time as thermoplastic materials do not require curing and can be recycled [15,22]. In a previous preliminary study De Carvalho and Amancio-Filho [15] demonstrated the feasibility of ultrasonically joining fully additively manufactured metal-polymer hybrid structures. Furthermore, De Carvalho and Amancio-Filho [23] showed that U-Joining can be used to assemble complex additively manufactured (AM) metal-polymer components, providing a novel manufacturing route for producing stronger and lighter hybrid structures. However, both studies highlighted knowledge gaps regarding the fundamental understanding of the joining parameters' influence on the mechanical performance and joint formation for AM U-Joints. Hence, in this paper, a Box-Behnken design of experiments (BBD) is applied to elucidate and correlate the effects of the joining parameters on the hybrid joint properties. The base materials 20%-short-carbon-fiber reinforced PEEK (PEEK-20CF) and 316L stainless steel (316L SS) were assembled and under single-lap shear test for this purpose. The joint formation, temperature development during the joining cycle, microstructural features, quasi-static mechanical and corrosion properties, and failure mechanisms were thoughtfully investigated to establish the scientific and engineering fundamentals of AM U-Joints.

1.1. U-joining

Three steps are involved in the U-Joining, as depicted in Fig. 1. Step 1 starts with positioning the parts between the sonotrode, where the tool is built, and the anvil, ensuring that the structured metal surface is in contact with the composite surface. In Step 2, the sonotrode applies vertical pressure and vibration to the parts, causing the high-frequency vibration to be converted into heat at the metal-polymer interfaces [24]. The mechanisms involved in this conversion are mainly the intermolecular friction in the polymer matrix (i.e. viscous dissipation) and the friction between the contact surfaces at the metal-polymer interfaces [25]. As a result, a portion of the polymer near the metal-fiber reinforced polymer interface is softened or melted, depending on whether the polymer is amorphous or semi-crystalline, allowing the TTRs insertion
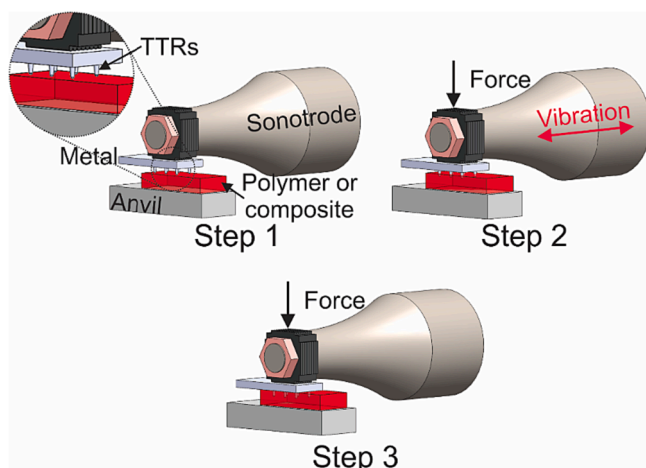
into the thermoplastic. De Carvalho et al. [24] described in a previous study that different vibration modes, such as horizontal and vertical, can be used in this step. However, as they observed, horizontal vibration generated more frictional heat at the metal-fiber reinforced polymer interface, which improved the polymer wettability and, consequently, the joint's mechanical performance. The TTRs are fully inserted into the composite in Step 3, and the vibration ceases, while the force is maintained until the solidification of the molten layer. This consolidation phase is essential to address the differences in shrinkage rates between the metal and the polymer, which may result in defects at the metal-fiber reinforced polymer interface. The sonotrode then retracts once the molten layer solidifies, completing the joining cycle [15].

The joint' out-of-plane mechanical properties are enhanced by the mechanical interlocking (due to the presence of TTRs) and adhesion forces [13,15,26]. Additionally, hybrid joints can improve their mechanical performance by applying protruding pins with complex forms, such as conical, convex, spherical or arrow-like heads [18,19,27]. Therefore, the TTRs geometry, density, and distribution can be customized according to the specific application requirements. Fig. 2-a) illustrates a few TTRs geometries that could be used for that purpose. The exploration of different geometries is beyond the scope of this study and will be investigated in the future.

Furthermore, Fig. 2-b) shows an example of a complex 316L SS/PEEK-20CF hybrid skin-stringer-bracket subcomponent manufactured by combining AM and U-Joining techniques. As discussed in the introduction and a previous study [23], both processes combined represent a novel manufacturing route to produce such lightweight and strong hybrid structures, which are interesting for transportation industries.

2. Materials and methods

2.1. Base materials, additive manufacturing techniques and u-joining setup

Laser powder bed fusion (LPBF) was used to print $15.5 \times 35 \times 3$ mm surface-structured 316L SS connectors with round-tip conical TTRs. The Creator RA (Coherent, Germany) LPBF equipment was used with pre-alloyed and gas-atomized spherical powder supplied by Carpenter Additive (USA). The LPBF parameters selected were based on literature [28] and included a printing speed of 1000 mm/s, layer height of 25 μm,
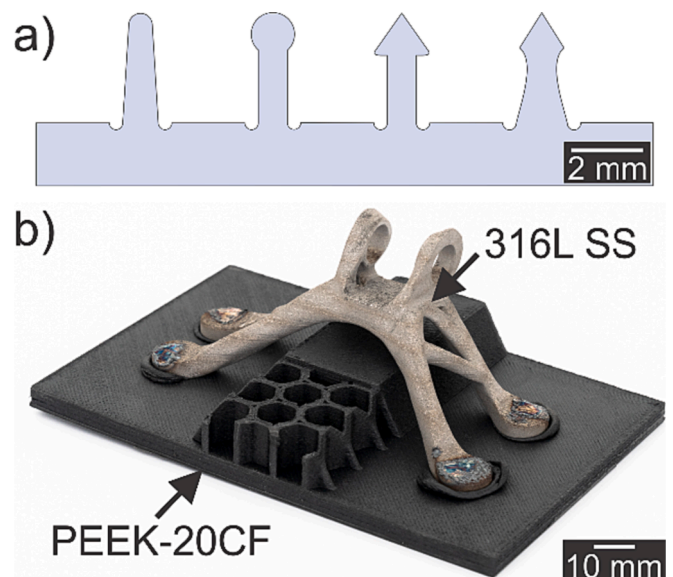

Fig. 1. Steps involved in the U-Joining process.

Fig. 2. Examples of a) different TTRs geometries and b) complex skin-stringer-bracket metal-fiber reinforced polymer hybrid subcomponent produced via the combination of AM and U-Joining techniques.

laser power of 120 W and laser spot diameter of 40 μm. The printed parts' chemical composition was determined via optical emission spectroscopy (OES) using a Spectrolab M8 (SPECTRO Analytical Instrument, Germany) spectrometer. The measured nominal values obtained are presented in Table 1 and match the typical values reported for this alloy [29]. Fig. 3-a) presents the connectors' dimensions and an overview of a produced joint used in this study. The selected TTR geometry was based on previous studies [13,23]. Additionally, a 0.2 mm undercut was added to the base of the TTRs to increase the joint mechanical performance by reducing the stress concentration in this region [26]. The influence of this TTRs geometry on the mechanical performance and fracture mechanisms of U-Joints was described in detail in a previous study [30].

Prior to joining, the influence of the building angle on the average surface roughness (S_a) of the LPBF 316L SS parts was assessed for five different angles: 0°, 30°, 45°, 60° and 90°. A VHX6000 digital microscope (Keyence, Japan) was applied for that purpose, where the upskins were analyzed. Additionally, the density of the printed components was measured according to ASTM B962-15 [31] using Archimedes' principle, resulting in a density of 7.8 ± 0.05 g/cm^3 or 98% compared to bulk material (8 g/cm^3 [29]).

Fig. 3-a) also depicts the dimensions ($15.5 \times 35 \times 6.35$ mm) of the flat fused filament fabricated (FFF) PEEK-20CF samples used in this study. These samples were produced using a FUNMAT HT (Intamsys, China) FFF equipment, employing a 1.75-mm-diameter filament supplied by 3DXTech (USA). The FFF parameters used were optimized in a previous study [32], where the PEEK-20CF mechanical properties were evaluated under three loading conditions: tensile, bending and impact tests. The selected parameters were: printing temperature of 385 °C, building plate temperature of 160 °C, building chamber temperature of 90 °C, layer height of 0.1 mm, and printing speed of 17.5 mm/s. Before each printing cycle, the building plate was coated with poly-vinylpyrrolidone (PVP) glue to improve the adherence of the component to the platform and avoid any warpage or deformation during the FFF process. Table 2 presents different physical and mechanical properties of the printed PEEK-20CF parts according to the filament manufacturer.

The joints were produced with an Ultraweld L20 (Branson Ultrasonics, USA) metal ultrasonic welding system using a fixed sonotrode vibration frequency of 20 kHz. The lap shear specimens (Fig. 3-a) were produced using the energy mode, where the sonotrode vibration is kept constant until the pre-set energy value is reached. Fig. 3-b) shows a side view of the same U-Joint, and Fig. 3-c) an overview of the tool marks left on the surface of the metallic part. As shown in Fig. 1, an exponential sonotrode was used, allowing a replaceable tool to be assembled on it. The tool applied in this study was manufactured via LPBF using the Carpenter Additive (USA) pre-alloyed and gas-atomized tool steel H13 spherical powder and printed in the Creator RA equipment (Coherent, Germany) using a laser power of 170 W, layer height of 25 μm, laser spot diameter of 40 μm and printing speed of 400 mm/s. Fig. 4 illustrates the geometry of the U-Joining tool used.

2.2. U-joining parameters optimization strategy

The U-Joining parameters were optimized via design of experiments (DoE) to produce strong joints with improved out-of-plane strength. DoE is an efficient and reliable method to assess the effect of process variables on a specific response and support analysis of their interactions [34]. A Box-Behnken design (BBD) model was followed in this study with three factors, i.e. three process parameters – joining energy (E_J), sonotrode amplitude (A_o), and joining pressure (J_P) – and three levels each, to analyze their influence on the ultimate lap shear force (ULSF)

response achieved by the produced single lap-shear specimens (Fig. 3). J_P is the cylinder pressure along the joining process in this study and its magnitude will be presented in pounds per square inch (psi) for convention. The experiments were conducted using a universal testing machine (Zwick/Roell Group, Germany) equipped with a 100 kN load cell, at room temperature and with a crosshead speed of 1 mm/min. Table 3 compiles the ranges (levels) used in the BBD experiments, which were selected based on the literature [15,26] and a previous screening investigation.

For three factors and three levels, the BBD requests 13 combinations of parameters, including the center point (i.e. $E_J = 5000$ J; $A_O = 75$ μm and $J_P = 37.5$ psi). The current study applied four additional center point replicates to enhance the accuracy of the model, resulting in a total of 17 joints produced and tested within the optimization process. The joints were randomly produced, and the used parameters and ULSF results are presented in Table 4.

The main objective of the BBD analysis is to define a combination of joining parameters capable of maximizing the reached ULSF and assembling joints free from visual defects such as lack of penetration, deflection or damage to the TTRs. The ULSF response achieved by the joined samples was thus used in an analysis of variance (ANOVA) to assess the model's fitting capabilities and identify the statistically significant parameters and their interactions [34]. A confidence level of 95% (i.e. $\alpha = 0.05$) was employed to evaluate the p-value test results. Additionally, the optimization process aimed at minimizing the E_J and J_P values used as an alternative to increasing the U-Joining tool lifespan. Previous studies have addressed this correlation and observed that both parameters play a major role in the observed tool wear [15,22,24].

2.3. Metal-fiber reinforced polymer interaction and thermal characterization

Wettability tests were performed at the surface of as-built 316L SS using 10 mg of PEEK-20CF filament to define their interaction by analyzing their contact angle. A Krüss DSAHT12 goniometer (HTM Reetz GmbH, Germany) was used in the study for three replicates. The system was heated until 400 °C (approximately 20% above PEEK's $T_m = 343$ °C) at a 10 °C/min rate, and kept constant at this temperature for 40 min, where the contact angle was then monitored and measured every 15 s. At the end of the test, the system was furnace cooled.

The study also monitored temperature development along selected joining cycles. Measuring the temperature accurately during U-Joining is challenging since the highest temperatures typically occur at the interface between the parts, which is not easily accessible. The polymeric material melts during the process, making it difficult to use thermocouples for temperature monitoring due to the complex environment created. Hence, infrared thermography was employed to monitor temperature development at both the tool/metallic connector and metallic connector/composite interfaces. For this purpose, an infrared thermo-camera (IR camera) produced by Variocam HD (Infratec, Germany), with a frame capture rate of 60 Hz, was utilized. The camera was positioned 0.3 m away from the sample area, directly facing the joining region, to enable the monitoring of temperature variations during the insertion of the first row of TTRs. To illustrate the placement of the IR camera, Fig. 5-a) and -b) present two schematic representations. Fig. 5-a) and -b) show two schematics to illustrate the positioning of the IR camera.

Table 1
Chemical composition of the LPBF 316L SS connectors. Reproduced with authorization from [24].

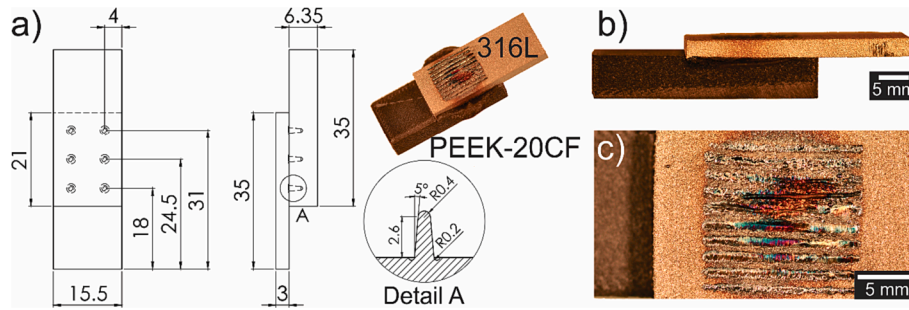| C	Si	Mn	Cr	Ni	Mo	S	N	V	W	Cu	Fe
0.03	0.76	0.73	17.97	13.67	2.29	0.01	0.05	0.04	0.01	0.04	Bal.

Fig. 3. A) geometry dimensions of the metallic connector (reproduced with authorization from [24]) and a joint overview, b) side view, and c) overview of a U-Joint. All dimensions are given in mm.

Table 2
Selected physical and mechanical properties of FFF PEEK-20CF [33].

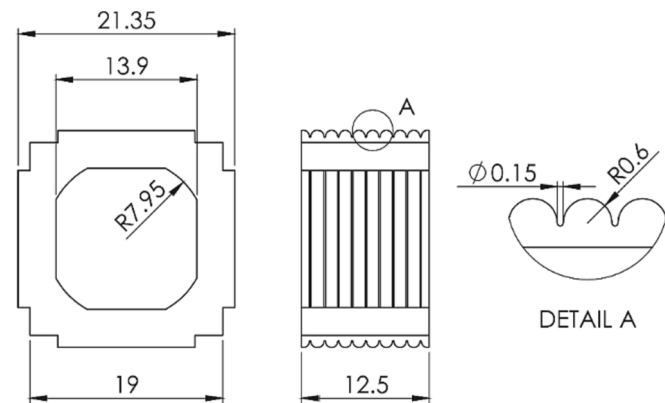| Density [g/cm^3]	Tensile strength [MPa]	Tensile modulus [MPa]	Elongation at break [%]	Flexural strength [MPa]	Flexural modulus [MPa]
1.39	126	10,100	1.9	145	11,200

Fig. 4. Dimensions of the U-Joining tool. All dimensions are given in mm.

Table 3
Joining parameters and their respective levels.

Parameter	Abbreviation	Low level low	High level
Joining energy [J]	E_J	2000	8000
Sonotrode amplitude [μm]	A_O	30	120
Joining pressure [psi/bar]	J_P	15/1	60/4.1

2.4. Microstructural and local mechanical properties analyses

Microstructural analyses were performed on selected specimens. Before the analyses, the samples were cut to produce cross-sections near the TTRs center, where the exposed surface was prepared following standard metallographic steps. The metal-fiber reinforced polymer interface was then examined using an Axio Observer 7 optical microscope (Zeiss, Germany). Vickers microhardness measurements were also performed on the polished surface to evaluate the effect and extension of the process-affected zone. The microhardness tests were performed following the ASTM E384-11 standard [35], using a load of 500 g, with a spacing of 0.5 mm between two adjacent indentations and applied for 15 s. Finally, scanning electron microscopy (SEM) was used to investigate the fractured surfaces of samples tested under quasi-static lap shear using a Tescan Mira 3 (TESCAN, Czech Republic). The specimens were carbon sputtered prior to the analysis, and the fractured surface was

Table 4
Box-Behnken design matrix and the achieved ULSF results.

E_J [J]	A_O [μm]	J_P [psi]	ULSF [kN]
2000	120	37.5	0.03
2000	75	15	0.12
5000	75	37.5	1.74
5000	75	37.5	1.35
5000	30	15	0.10
8000	120	37.5	2.54
2000	75	60	1.64
5000	120	60	3.56
5000	75	37.5	1.70
5000	120	15	0.85
5000	75	37.5	2.45
8000	75	60	2.40
8000	75	15	0.01
8000	30	37.5	0.04
5000	30	60	0.33
5000	75	37.5	1.55
2000	30	37.5	0.13

investigated using the backscattered electron detector with a chamber pressure of 10^{-1} Pa and an acceleration voltage of 10 kV.

2.5. Electrochemical corrosion tests

To evaluate the effect of U-Joining in the AM 316L SS corrosion resistance, a potentiodynamic polarization test in a naturally aerated solution of 3.5 wt% sodium chloride (NaCl) at 25 °C was carried out [36]. The analyses focused exclusively on the metal surface and not the metal-fiber reinforced polymer interface, as this is the region exposed to the environment, and the combination of stainless steel and carbon-fiber-reinforced polymer does not form a galvanic couple [37,38]. Three conditions were selected for this analysis: the as-built material, and joined samples with optimized parameters and with a higher energy input in comparison to the optimized specimens. The exact parameters for both samples will be presented later during the optimization discussion. The measurements were taken using a Reference 3000 (Gamry, USA) potentiostat and analyzed in the Gamry Echem Analyst (Gamry, USA) software. The electrochemical cell used consisted of a reference electrode composed of silver/silver chloride (Ag/AgCl) in saturated KCl solution, a platinum sheet (area of 5 cm^2) counter electrode and a Ø 10 × 3 mm (surface area of 0.7854 cm^2) working electrode extracted via water jet cutting from the metallic component of the joined region marked by the U-Joining tool (Fig. 3-c). The dashed lines in Fig. 6-a) indicate the position from where the working electrode was extracted. For each working electrode extracted, the attached PEEK-20CF was removed, and the lateral sides and edges were polished and protected with nail polish to avoid crevice corrosion in undesired regions. Once dried, a copper wire (AWG 35) was mounted onto the opposite surface using a silver paste to establish electrical contact. Subsequently, the system was insulated with polyester resin, leaving the area marked by
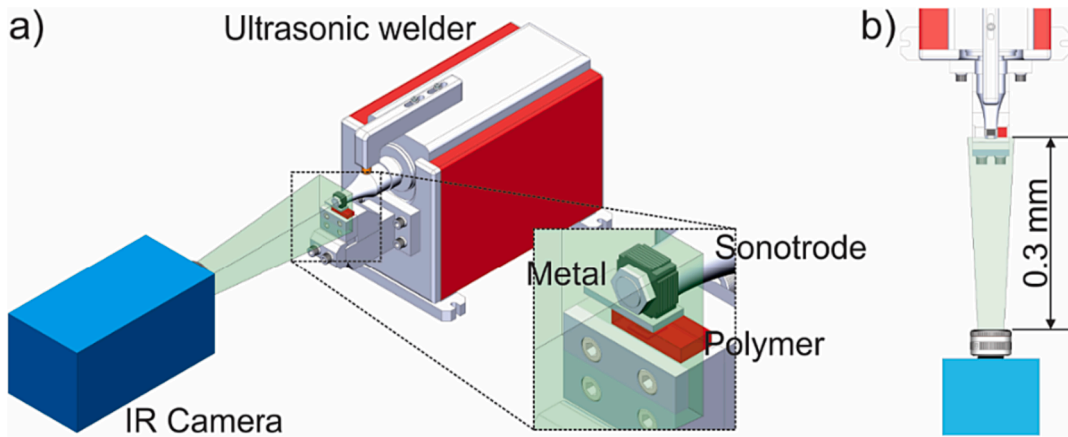
Fig. 5. A) schematics of the infrared camera setup concerning the joint parts and b) distance between the ir camera and the measurement area.
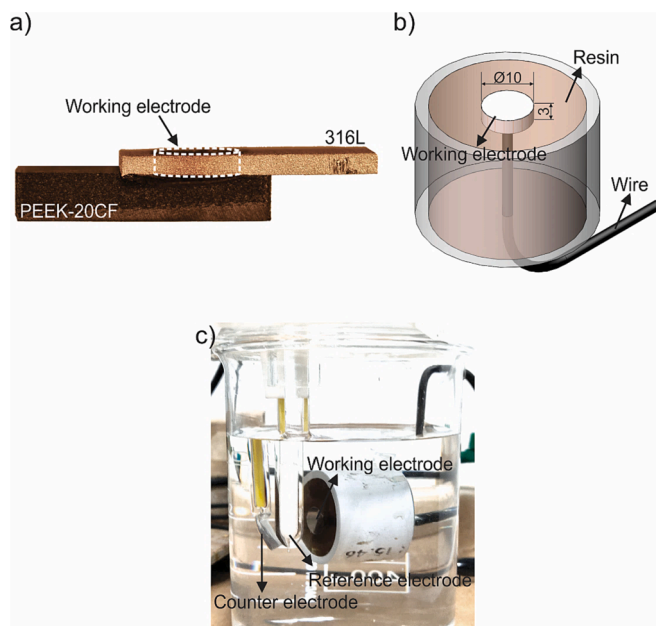

Fig. 6. A) region from where the working electrode was extracted; b) schematic illustration of the working electrode assembly and c) experimental cell used for the electrochemical polarization tests. all dimensions are given in mm.

the joining tool exposed for analysis. Fig. 6-b) and -c) show a schematic of the working electrode and the experimental working cell mounted, respectively. Before the measurements were made, the exposed area on each working electrode was carefully polished, washed and then immersed in the electrochemical cell. Following immersion in the solution, the samples were left in an open circuit condition for 3600 s (60 min) to reach a steady-state potential known as the open circuit potential (E_{oc}).

The potentiodynamic polarization tests started at 300 mV below E_{oc} and proceeded with a scan rate of 1 mV/s. The tests were stopped upon reaching the pitting potential (E_{pit}) to prevent further localized corrosion attack. The E_{pit} values were recorded as the potential at which a sudden and significant increase in current density occurred and reached a value exceeding 100 μA/cm^2 [39]. The average values of E_{pit} and corrosion potential (E_{corr}) were derived from three separate measurements, and the standard deviation was calculated. Following the corrosion tests, selected polished samples were analyzed to identify surface corrosion morphology using a Tescan Mira 3 scanning electron microscope (TESCAN, Czech Republic).

3. Results and discussion

3.1. General aspects of LPBF parts and physical–chemical interactions between AM 316L and PEEK-20CF

General aspects of the applied materials were assessed before the joining process, and the printing conditions and interactions were defined. Several rules related to overhang designs are described in the literature for LPBF 316L SS parts when using commercially available powders. These constraints limit the way parts are built and can illustrate the effects of building angles on different properties. Thomas [40] demonstrated that the printing quality of overhangs parallel to the building platform is affected to an extreme extent if the overhang exceeds 1.5 mm in length for 316L SS, making support structures necessary. Piscopo *et al.* [41] demonstrated that the building angle strongly affects the surface roughness of LPBF printed parts for building angles between 35° and 90°. Since the surface condition plays a strong role in the micromechanical interlocking and adhesion mechanisms of metal-fiber reinforced polymer hybrid joints [11], the present study initially assessed the influence of the building angle on the average surface roughness (S_a) of the upper surface of LPBF 316L SS parts by analyzing five different angles: 0°, 30°, 45°, 60° and 90°. The obtained results are summarized in Fig. 7.

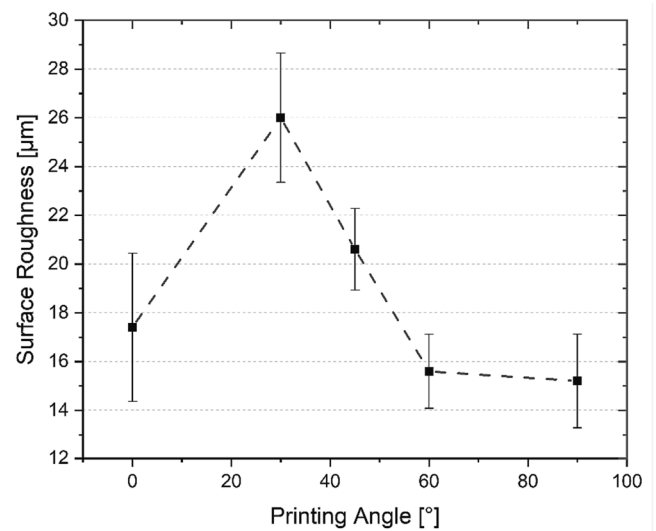As can be seen, the building angle can strongly influence S_a. For parts

Fig. 7. Effects of the building angle on surface roughness of 316L SS parts printed via LPBF.

printed at 30°, the highest S_a values are reached. Wang *et al.* [42] observed similar behavior for the same material and defined that a surface with an inclination of less than 35° starts to present a strong stair-stepping effect, which increases S_a. Calignano [43] also showed that this increment in S_a for low building angles (<35°) primarily results from the presence of partially fused particles that adhere to the molten component. Additionally, when applying building angles below from 0° to 30°, the printing parts must be sustained entirely with support structures on the bottom surface to not collapse, resulting in two effects: smoothing S_a of the upper surface due to the direct laser incidence, and worsening S_a of the bottom surface due to the downskin effect [43]. These two effects explain the observed S_a values for 0°. On the contrary, parts printed with a building angle > 60° did not present any of these issues, as the stair-stepping and downskin effects are minimized, reducing the parts' S_a. De Carvalho and Amancio-Filho [15] showed that higher S_a can improve the micromechanical interlocking in metal-polymer hybrid joints produced via U-Joining, which indicates that a build angle between 30 and 45° would be ideal for the present application. However, since printing at 30° would require the use of support structures, a building angle of 45° was selected for this study.

After establishing the conditions for the LPBF samples, wettability tests between the 316L SS printed at 45° and PEEK-20CF were performed at high temperatures to establish their physical–chemical interaction qualitatively. The obtained results are summarized in Fig. 8.

The results show that the contact angle between both materials is generally higher than 100° for the analyzed conditions, indicating a hydrophobic behavior of the solid surface, as described in the adsorption theory [44,45]. As presented by Zhang *et al.* [45], rough surfaces increase the effective surface area, which benefits the wettability of the parts, reducing the contact angles (approximating to a hydrophilic behavior with angles between 0° and 90°). However, the rough surface of the as-built 316L SS was insufficient to reach such low angles. Two theories could explain this behavior: (i) the inherent surface energy of the rough adherend (AM metal), which is lower than the level of a smooth-surfaced – i.e. reduces the difference to the surface tension of the polymer and diminishes their wettability [45], and (ii) the presence of entrapped gases inside the metal surface cavities, which results in a solid–liquid-gas three-state contact that prevents the molten polymer from penetrating downwards [45]. Both cases prevent complete surface wetting, resulting in poor adhesion forces, which can diminish the global mechanical performance of metal-fiber reinforced polymer hybrid joints [45]. Since the present study does not aim to explore surface treatments that could improve the metal-fiber reinforced polymer surface energy correlation, it is important to guarantee that an optimized joining parameter set is applied during the U-Joining process, ensuring that the necessary joining pressure and temperature are reached to allow the polymer to flow and fill those surface cavities, improving surface wetting and, consequently, the micromechanical interlocking, as well as possible primary chemical bonds between the metal and the composite, as reported in the references [46].

3.2. U-joining process parameters optimization

The U-Joining process parameters were optimized to promote an improved metal surface wetting and ensure a strong connection between the parts, maximizing the joint's mechanical performance. By following the BBD and ANOVA presented in Section 2.2. and using the ULSF results presented in Table 4, a reduced statistical model could be obtained. This model allowed for the determination of the influence of each joining parameter on the strength of the joint, thereby defining their respective contributions. The terms and their interactions considered statistically

Table 5
Statistically significant terms for ULSF and their corresponding p-values.

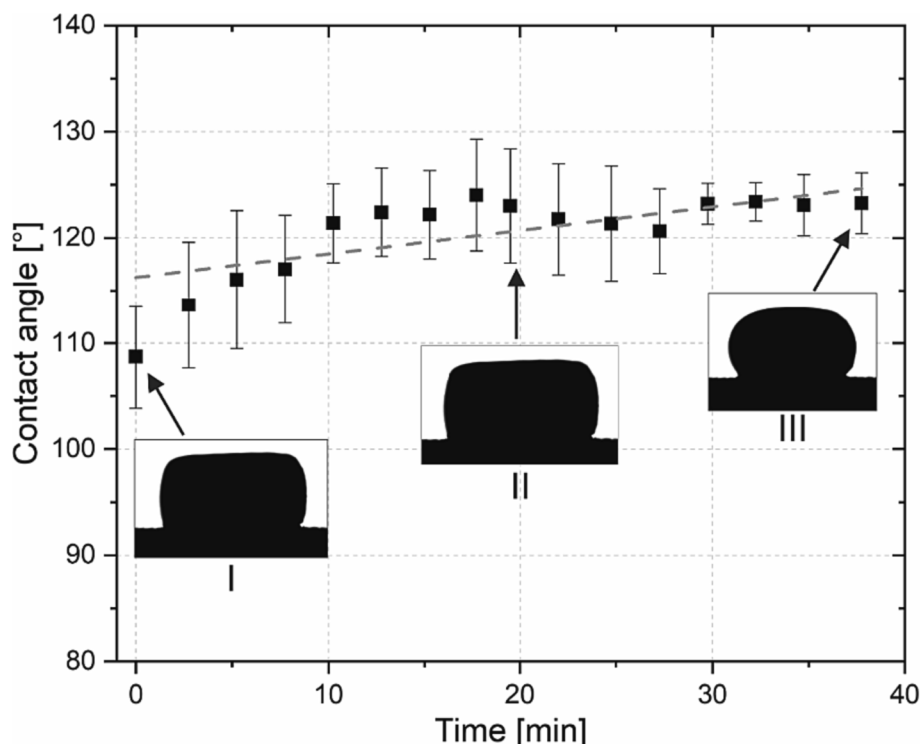| Parameter	p-value
J_P	0.001
A_O	0.001
E_J^2	0.026
E_J*A_O	0.029
A_O*J_P	0.036

Fig. 8. Contact angle variation of PEEK-20CF on 316L SS surface at 400 °C.

significant (with a p-value lower than 0.05) were identified and are summarized in Table 5.

As can be seen, the results show that two main parameters and three interactions had statistically significant impact on ULSF: J_P and A_O main effects; E_J^2 second-order interaction effect, as well as the two-way interaction effects $E_J * A_O$ and $A_O * J_P$. These effects can also be graphically represented on a Pareto chart of standardized effects (shown in Fig. 9), which can include their respective synergic (positive) or non-synergic (negative) behaviors, facilitating the discussion. The effects are arranged in decreasing order of relevance, with each bar's length indicating its standardized effect or interaction – calculated by dividing the effects of the analyzed parameters and interactions by their standard error. Here the relevance threshold is marked by the vertical dashed line, indicating the parameters that are statically significant at a confidence level of 95%. Any bar crossing line suggests that the corresponding parameter has a significant impact on the considered ULSF response. The influence of the non-statistically significant E_J main effect (p-value of 0.06) was also included here to illustrate its behavior and magnitude.

J_P and A_O main effects showed the strongest influence on the ULSF, presenting a synergic effect. Consequently, increments in their values will strongly improve the ULSF of the produced joints. E_J also presented a positive behavior, but did not reach the relevance threshold, meaning that its influence could be ignored from a statistical point of view. However, from an engineering perspective and as discussed later, E_J strongly influences the resulting joining time and energy input, influencing not only the ULSF reached, but also the observed U-Joining tool wear and the temperatures reached during the joining cycle. In summary, the findings reveal that ULSF generally rises with high J_P and A_O values, and that both have a greater influence than E_J. These results contradict those reported in the literature for U-Joining of laminated glass-fiber reinforced polyetherimide (PEI) and metal injection molded (MIM) Ti-6Al-4 V [26]. In their study, Feistauer *et al.* [26] observed that J_P was not a statistically significant parameter. As observed and discussed in Fig. 8, this difference is mostly due to the lower surface energy of the AM metal (compared to a smooth-surfaced part) and its high surface roughness, which prevents a complete surface wetting and influences the presence of entrapped gases at the interface. Therefore, J_P seems to play an essential role in joining AM parts by forcing the molten polymer to fill surface cavities of the rough AM 316L SS part, thereby improving the micromechanical interlocking between the parts and, consequently, the mechanical performance of the joint. Additional discussion between the parameters interactions will be presented below.
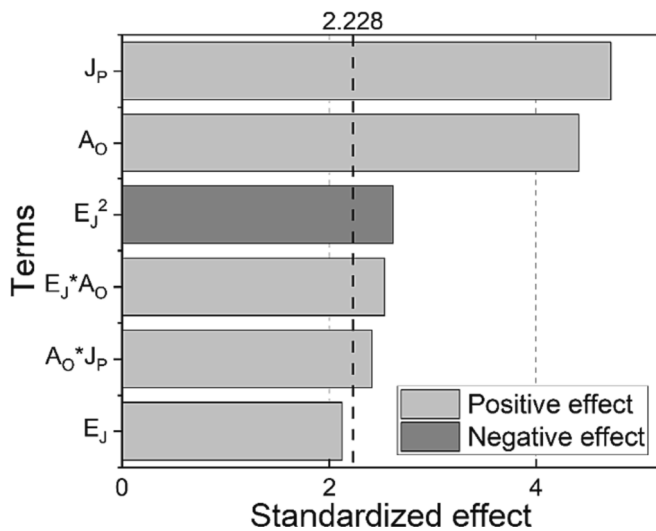
Apart from the p-values obtained, the statistical investigation generated a reduced regression model capable of predicting ULSF, and the parameter indices in the model can be used to evaluate its explanatory power. The backward elimination technique with $\alpha = 0.05$ was used to obtain the reduced model, which is shown in Equation 1. This equation expresses the ULSF response as a function of the applied joining parameters.

ULSF [kN] = -0.16 + 0.00049*E_J-0.0293*A_O-0.0079*J_P-0.000000077*E_J^2 + 0.000005*$E_J * A_O$ + 0.000612*$A_O * J_P$ (1).

Fig. 10 compares the experimental ULSF and the model predictions using Equation 1. Further validation points were randomly joined and tested, and the obtained results were also included.

Fig. 10 10 indicates that all design points are within the 95% confidence interval of the model, showing that the model correlates well with the experimental data and can fit the values within the analyzed ranges. The model's adjusted and predicted R-squared values were 86.75% and 78.8%, respectively, with a standard error (S) of 0.51 kN. According to Myers *et al.* [34], a difference of less than 20% between the adjusted and predicted R-squared values indicates that the model fits the data well and can estimate other values within the analyzed parameter ranges. Since the phenomena involved in friction-based joining processes are so complex and due to the presence of defects in AM parts, the achieved results were deemed satisfactory.

The obtained regression Equation 1 can also be used to prepare contour plots to illustrate the pair interaction effects between the parameters, with the third fixed on the center value. The obtained graphs are illustrated in Fig. 11.

The contour plots indicate that joints produced with an E_J below 5000 J achieve lower mechanical performance (between 1.4 kN and 2.1 kN), when considering the E_J interactions with J_P (Fig. 11-a) and A_O (Fig. 11-b), respectively. This behavior can be related to insufficient heat input resulting in low heat generation and lack of TTR penetration [15]. De Carvalho and Amancio-Filho [23] addressed the combination of AM 316L SS and unreinforced PEEK in a previous exploratory study, where they observed that high E_J values could lead to higher temperatures during the joining process, increasing the polymer heated-affected zones and initiating the thermal decomposition of the polymer in the overlap areas. However, Fig. 11 does not indicate a similar behavior for the explored range, as the achieved mechanical performance would appear to be stable for E_J between 5000 and 8000 J – when J_P (Fig. 11-a) and A_O (Fig. 11-b) are fixed at 60 psi and 120 μm, respectively. This plateau will later be associated with the failure mechanism observed for the parts: a mixture of adhesive, cohesive and net tension from the PEEK-20CF side, which indicates that the limits of the polymeric part were reached before the failure of the joint. As aforementioned, one of the main goals of this study is to minimize E_J without diminishing ULSF, to minimize the observed U-Joining tool wear. Therefore, the present study selected an E_J of 5000 J as the optimum value. This E_J also corresponds to the process parameter value of the center point runs.

On the other hand, the interaction between J_P and A_O (Fig. 11-c) exhibited a well-defined range of maximum ULSF (above 3.5 kN) when the highest values are applied for both parameters, and E_J is kept constant at 5000 J. As discussed in a previous publication [15], this behavior is related to the fact that higher amplitudes (combined with the high sonotrode frequency) increase the energy input during the joining cycle, facilitating the melting process of the PEEK matrix. A high J_P value will force the metallic surface against the molten PEEK, squeezing the polymer against the metal surface and filling its surface cavities. The result after the polymer consolidation is a strong joint with combined effects of micromechanical interlocking and adhesion forces generated at the metal-polymer interface. In conclusion, the selected optimized U-Joining parameters were: E_J of 5000 J, A_O of 120 μm and J_P of 60 psi, resulting in a ULSF of 3.6 ± 0.3 kN. The resulting joining time for this condition is approximately 3 ± 0.3 s, without considering the polymer consolidation time (Step 3 in Fig. 1). This study used an overlong consolidation time of 30 s for all the analyzed conditions to compensate
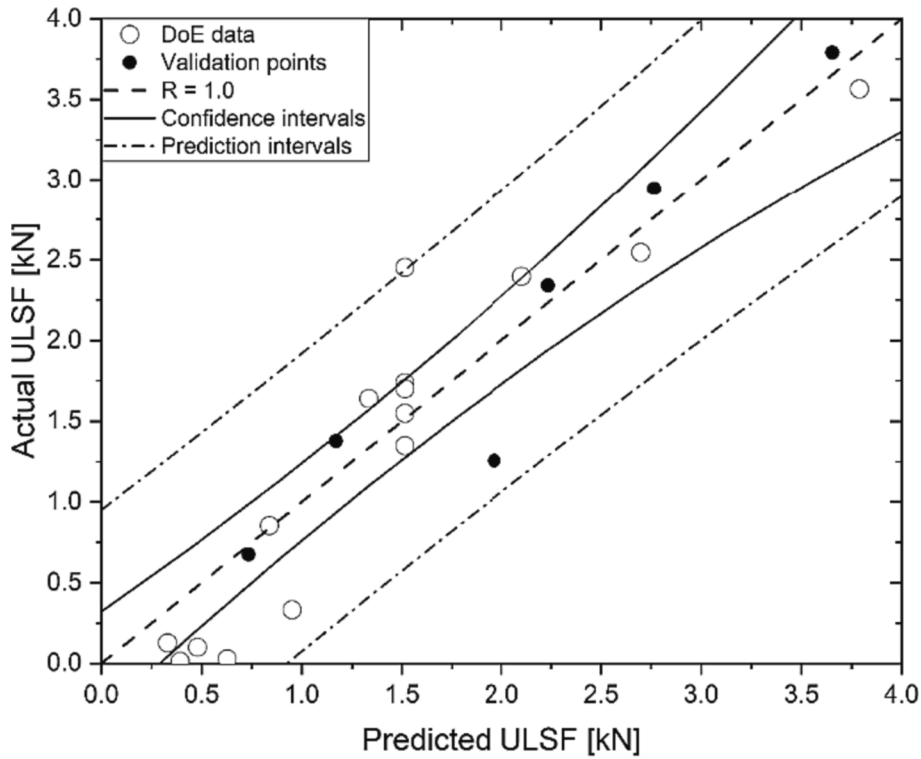

Fig. 9. Pareto chart of standardized effects highlighting significant factors (process parameters), interactions and their influence on ULSF of AM hybrid joints produced by U-Joining.

Fig. 10. Actual versus predicted diagram for the ULSF obtained from the BBD statistical model (Equation 1).
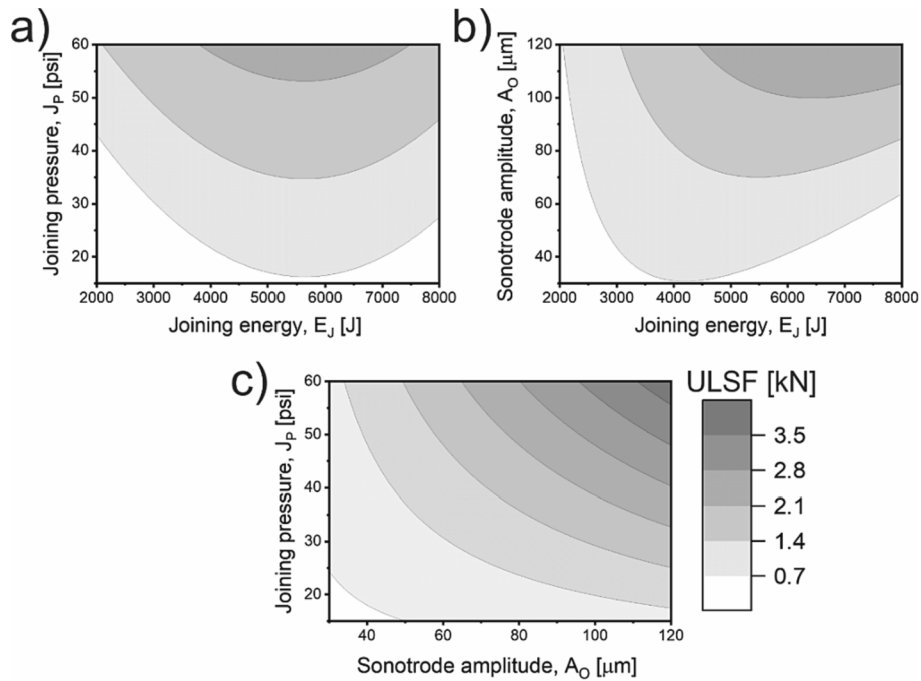

Fig. 11. Obtained contour plots of two-way interactions between the analyzed parameters for the ULSF response: a) $E_J \times J_P$; b) $E_J \times A_O$ and c) $A_O \times J_P$.

for any polymer shrinkage during cooling. A study to reduce this consolidation time was out of the scope of this scientific study, but is planned for the future.

3.3. U-joint formation mechanisms of AM materials and general aspects

As previously stated, a U-Joint is produced by using high-frequency vibrations at low amplitudes on the metal-fiber reinforced polymer interface, which softens the thermoplastic matrix, allowing the TTRs insertion. Consequently, intense heat generation and dissipation can be observed in a fraction of a second, combined with localized material flow (due to the TTRs penetration). Therefore, a systematical and step-wise stop-action study was conducted to understand the joint formation using the optimized parameters set identified in the previous step. Five different joints were produced with fixed A_O of 120 μm and J_P of 60 psi values, but with incremental E_J: 1000, 2000, 3000, 4000 and 5000 J.
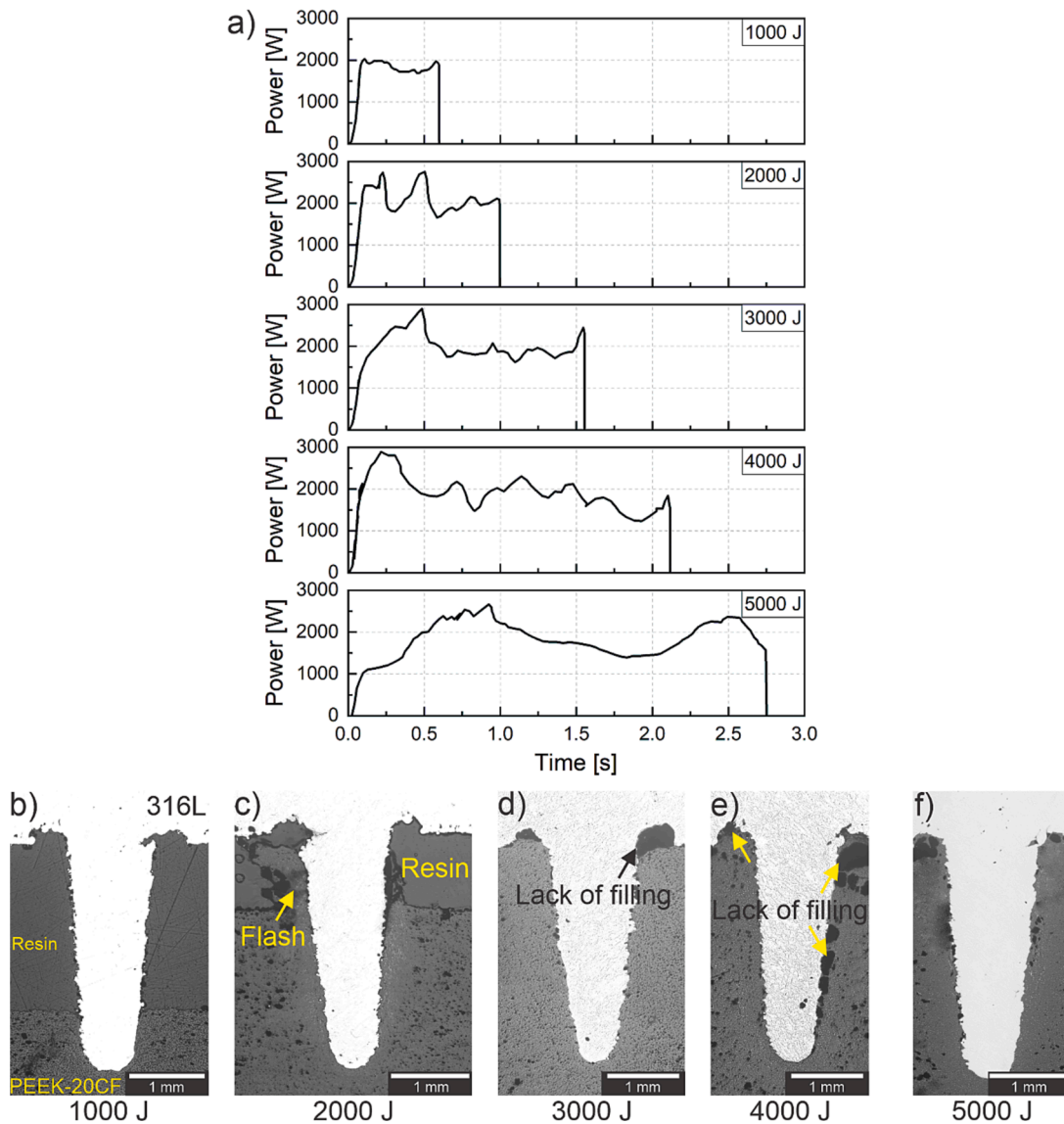
Fig. 12. Stop-action analysis where a) presents the time × power curves for the five analyzed joining energy (E$_J$) conditions and b) - f) the cross-sections showing the TTR insertion for the same E$_J$ different levels.

Fig. 12-a) shows representative time × power curves for all the five conditions. As defined by Benatar [47], the joining device operates in a closed loop, wherein the ultrasonic transducer's power is measured and then integrated over the joining cycle until it reaches the E$_J$ pre-set value. This integration corresponds to the area under the time × power curve. As a result, joining time increases with E$_J$ increments. The curve for 5000 J also confirmed that the joining cycle for the optimized condition is within 3 ± 0.3 s. Fig. 12-b) to -f) show cross-sections showing the TTR insertion for the same E$_J$ different levels.

As one can see, an E$_J$ of 1000 J (Fig. 12-b) is not enough to generate the necessary heat at the interface between the TTRs and the PEEK-20CF part, restricting their insertion. Since a solid–solid system is observed, this can be correlated to the beginning of the curves presented in Fig. 12-a), where there is a sudden increase in power as a result of the application of normal force and vibration. The main heat generation mechanism in the process is attributed to the Coulomb or solid friction phenomenon, where heat is produced due to frictional forces between the surfaces of the joining materials [48,49]. At an E$_J$ of 2000 J (Fig. 12-c), additional heat is generated by the friction between the polymeric chains (i.e. intermolecular friction) and the parts. This leads to a temperature rise that is sufficient for localized melting of the polymer matrix

located beneath the TTRs. Consequently, the viscosity of the polymeric matrix decreases, allowing the insertion of the TTRs [50]. In Fig. 12-c) it can also be seen that the penetration creates a softened polymer outflow (i.e. flash) at the interface. This transition from a solid to a molten state and heat dissipation results in an unsteady heat generation at the beginning of this insertion, which clarifies the strong fluctuations in the power curve for this condition.

The heat generation for higher E$_J$ levels (such as 3000 and 4000 J) becomes more stable, leading to a solid-molten state where a larger volume of molten PEEK forms around the vibrating TTRs. According to Feistauer [22], at these E$_J$ levels, there is a balance between the rates of polymer melting and molten material outflow, leading to an equilibrium between heat input and heat outflow. This equilibrium accounts for the decrease in power levels observed towards the end of both 3000 and 4000 J curves (Fig. 12-a). Although the TTRs are already fully inserted at E$_J$ of 3000 and 4000 J, Fig. 12-d) and -e) show a high number of defects (such as lack of filling) at the base of the TTR and the flat metal-fiber reinforced polymer interface, indicating that the portion of the molten polymer was not enough to wet the whole rough surface of the metallic part. To fill these voids, E$_J$ must be increased to 5000 J. In this case, TTRs are fully inserted into the PEEK-20CF and restrained by the surrounding

polymeric material, resulting in increased resistance to vibrational motion. To overcome this resistance, there is an increment in the electrical power to maintain the constant sonotrode vibration, as shown at around 2.5 s of the curve presented for 5000 J in Fig. 12-a). The additional energy input allows the melting of an additional portion of the polymer, which will be compressed by the metallic part and forced against its surface, wetting the residual regions (as shown in Fig. 12-f). The squeezed material will also form a flash on the sides of the overlapping area, as presented in Fig. 3-a).

A similar behavior in the context of the joint formation mechanisms were observed by Feistauer [22] for MIM Ti-6Al-4 V and laminated glass-fiber reinforced PEI. However, in his study, the energy input necessary to produce strong joints was significantly lower than the ones in the present manuscript (i.e. $E_J = 2012$ J; $J_P = 14.7$ psi; $A_O = 52$ μm). This difference suggests that the high surface roughness presented by LPBF parts demands higher energy inputs to guarantee that the joint is
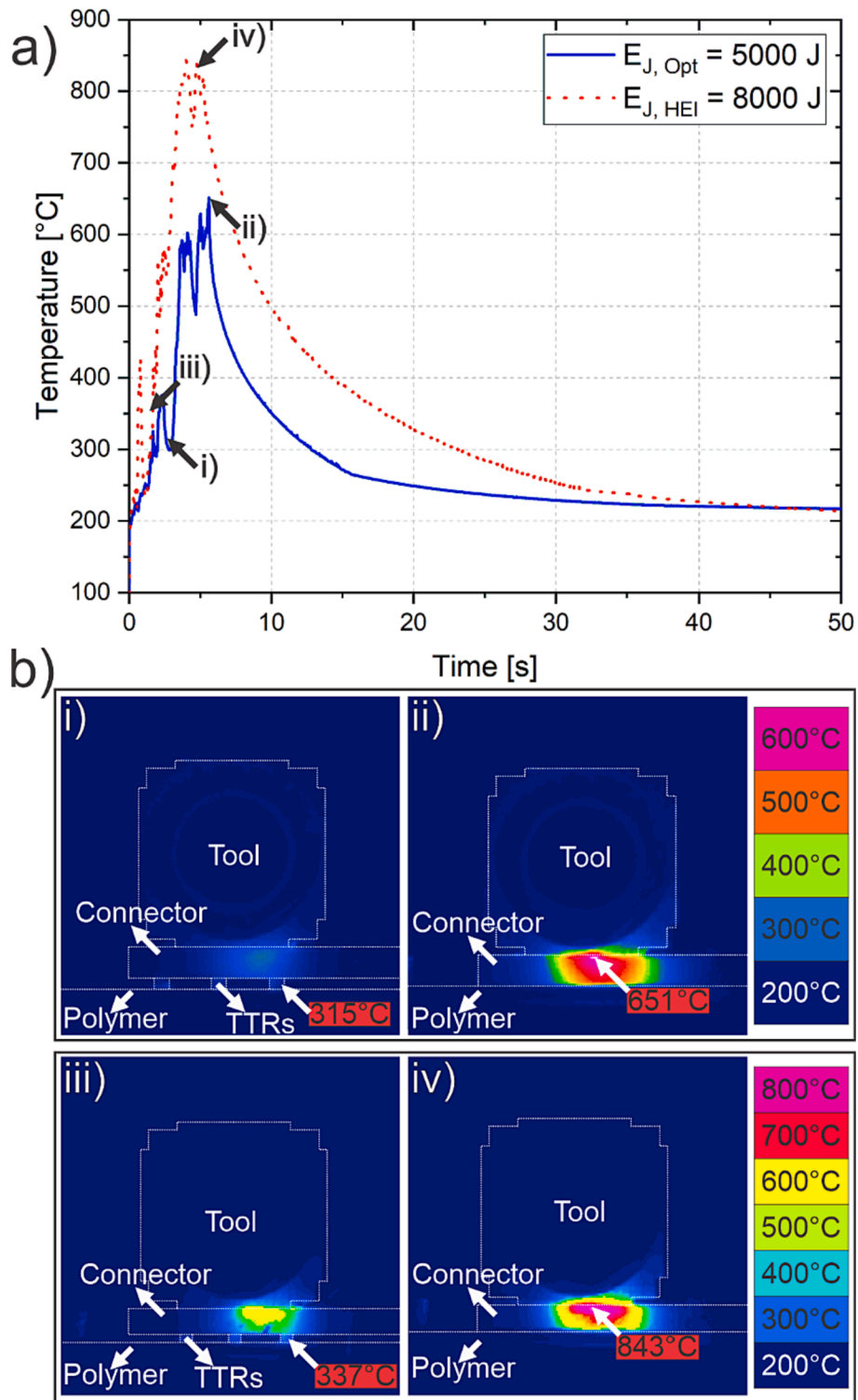

Fig. 13. A) temperature development throughout the u-joining process and b) temperature distributions: i) and iii) at the beginning of the process for the optimized and hei conditions, respectively; and ii) and iv) after the ttrs have been completely inserted for the optimized and HEI conditions, respectively.

completely formed, ensuring the high mechanical performance of the joints. Furthermore, as showed in Fig. 11, higher E_J values would not improve ULSF, as the maximum macro- and micromechanical anchoring is already reached. In other methods of joining materials through friction, it is widely recognized that above a certain level of energy input, further increases only lead to higher temperatures during the joining process. This, in turn, can result in thermal flaws and thermomechanical degradation of the polymeric material [51–53], in addition to higher tool wear [12,15]. Finally, it is worth mentioning that after this point (E_J of 5000), some of the energy input may be dissipated through friction between the metallic part and the joining tool.

The temperature development during the joining cycle can also provide relevant information to understand the joint formation mechanisms. Staab and Balle [54] and De Carvalho and Amancio-Filho [15] showed that ultrasonic joining processes for hybrid joints generate friction between the joining tool and the metallic part, which increases the temperature of the joining region. The temperature rise must be monitored to avoid the polymer's thermal degradation or decomposition, which could reduce the mechanical performance of the joint, as observed by Abibe *et al.* [53]. Therefore, the process temperature was also monitored to support understanding. Two representative IR-temperature development curves recorded during the joining cycle are presented in Fig. 13-a): one for the optimized condition (E_J of 5000 J), and one for higher energy input, HEI (E_J of 8000 J). The curves indicate that the temperature development is marked by a steep rise at the beginning of the joining process, which can be correlated to the abrupt power increase early in the process (Fig. 12-a). The temperatures reached here depend entirely on the joining parameters, since higher energy inputs result in higher joining temperatures. The maximum values registered for the optimized and HEI conditions confirm this, as they reached 638 ± 82 °C and 864 ± 30 °C, respectively.

As previously described, during the initial stages of the ultrasonic joining process, energy transfer from the sonotrode to the metallic connector occurs easily as the TTRs are not yet inserted and act as energy directors. This results in the development of frictional heat near the TTRs, as shown in Fig. 13-b-i) and -b-iii) for both conditions – optimized and HEI, respectively. At this point, the temperature at the TTRs is already higher than PEEK's glass transition temperature ($T_g = 143$ °C [55]). The combination of high temperature and sonotrode pressure causes the upwards flow of the softened material, facilitating the insertion of TTRs. Once the TTRs final position is reached, the metallic connector is anchored by the fixed polymer, making it difficult for energy transfer to occur due to slippage between the tool and the metallic connector, as described in Fig. 12. This situation results in the maximum temperatures recorded along the joining process, which are illustrated in Fig. 13-b-ii) and -b-iv).

A previous feasibility study for 316L SS and PEEK used non-optimized U-Joining process parameters and registered maximum temperatures within the joining cycle higher than 830 °C [15]. This study presented the possibility of reducing the temperatures reached via parameters optimization as a possible solution. This proposition could be confirmed here, since it can be clearly observed that the maximum temperature was reduced by approximately 200 °C when an optimized E_J of 5000 J was used (Fig. 13-a). This reduction in the temperatures reached is extremely important for the process development, as it reduces the chances of thermal decomposition at the polymer side. According to Patel *et al.* [56], PEEK starts to degrade from 500 °C to 600 °C due to random chain scission of the ether and ketone bonds, which forms phenol, preferentially. The second mechanism occurs between 600 °C and 800 °C, where the decomposition products undergo recombination through crosslinking, resulting in reduced phenol volatilization. Therefore, since the maximum temperature was recorded at the joining tool/metallic connector interface, and since Fig. 13-b-ii) shows that the temperature at the metal-fiber reinforced polymer interface is much lower (around 400 – 500 °C) for the optimized condition, one can expect that the chances of polymer degradation were reduced. Nevertheless,

further investigation is necessary to evaluate these effects and will be conducted in the future.

As mentioned before, the micromechanical interlocking and the presence of defects at the metal-fiber reinforced polymer interface influence the mechanical performance of the joint. Therefore, additional microstructural analyses were conducted to evaluate the quality of the joint. Fig. 14-a) illustrates a typical cross-sectional view of an optimized joint, including microstructural details of two distinct areas.

Fig. 14-a) confirms the full insertion of TTRs into the composite component, and also shows that the combination of frictional heat and TTR insertion resulted in the formation of a thermo-mechanical affected zone (TMAZ) near the metal-fiber reinforced polymer interface. Since short fibers were used, a proper reorientation due to molten polymer flow and joining pressure could not be observed, and the fibers were randomly reorganized. Additional fiber breakage could also not be identified in this analysis. In Fig. 14-b) and -c), a pronounced micromechanical interlocking is observed between the rough surface of the 316L (light grey) and PEEK-20CF (dark grey). Both images also illustrate how molten PEEK could flow around particles adhered to the metallic surface and fill surface cavities, indicating that the joint has a better micromechanical strength than a smooth-surfaced metallic specimen. The yellow arrows indicate the presence of a reduced occurrence of volumetric defects at the interface. This reduction can be attributed to two distinct phenomena: (i) residual porosity of FFF printed parts, resulting mainly from intra and inter-bead voids, and (ii) thermally-induced defects, as the presence of entrapped gases during polymer solidification after joining, which can be products of thermal decomposition or moisture evolution [57]. Since higher energy inputs did not improve the mechanical performance of the joint, and since the presence of defects was also reported for laminated composites [22], it can be expected that eliminating these defects is virtually impossible without using additional post treatments – e.g. hot isostatic pressing [58,59].

The effect of the joining cycle on the local mechanical properties of 316L SS was assessed by Vickers microhardness profiles, where as-built, optimized and HEI joints were analyzed and are presented in Fig. 15. All the measurements were performed on cross-section materiallographic samples, 0.5 mm away from the upper surface of the 316L SS connector (which was in contact with the joining tool), across the regions where the TTRs were located. The dashed line presented in the inlet image illustrates the position from where the measurements were taken. By comparing all three profiles, no apparent process-related changes in hardness distribution could be observed, even for the HEI specimen. The averaged values confirm this, since the as-built, optimized and HEI samples reached similar values: 233 ± 7; 227 ± 7 and 221 ± 8, respectively. These results are in accordance with what was observed by Feistauer [22], where no changes induced by the U-Joining process were seen in the metallic connector, except for the deformations left by the U-Joining tool on its surface (Fig. 3-a).
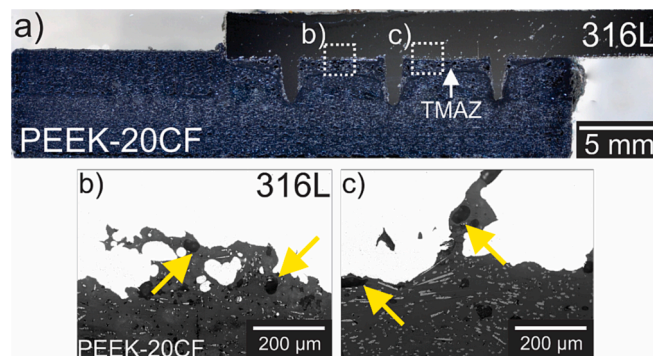

Fig. 14. A) a view of the cross-section of an optimized u-joining 316l/peek-20cf hybrid joint; b) and c) depict details of the metal-polymer interface. joining conditions: e$_J$ of 5000 J, A$_O$ of 120 μm and J$_P$ of 60 psi.
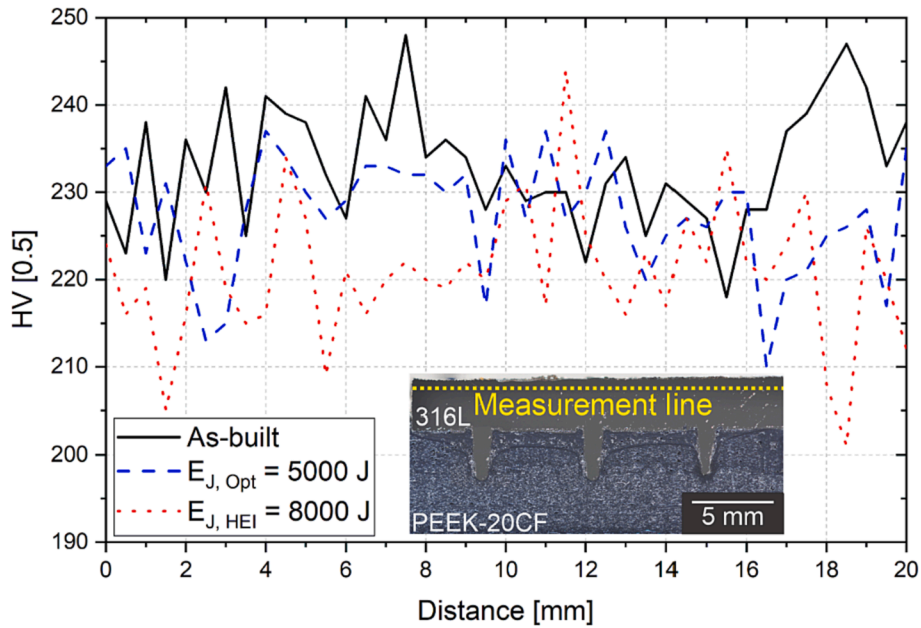
Fig. 15. Microhardness profiles from three specimens: as-built and joints produced with optimized and higher energy input (E_J of 5000 and 8000 J, respectively).

The previous discussions described the U-Joint formation mechanisms demonstrating the importance of the TTRs during the joining cycle, as they act as energy directors. However, the improvements brought by their addition can also be evaluated by comparing the obtained mechanical performance results with pinless reference samples, printed and joined with the same optimized conditions and dimensions to keep the same energy input and allow a direct comparison between the obtained values. Fig. 16-a) demonstrates the global mechanical performance for both conditions by presenting a typical force––displacement curve under lap shear testing for a U-Joint and a pinless joint. Fig. 16-b) and -c) depict fractured samples for both conditions, respectively.

The results demonstrate that strong joints are formed for both conditions. The achieved values also indicate an increase in the ULSF from 1.4 ± 0.2 kN to 3.6 ± 0.3 kN (2.6 times) and for the displacement at break (DaB) from 1.2 ± 0.3 mm to 2.4 ± 0.1 mm (2 times) when comparing U-Joints and pinless-reference joints. The increased area beneath the curve also implies that the U-Joints have a higher damage tolerance. These findings are consistent with previous research, as

different studies have already shown that including TTRs enhances the damage tolerance and mechanical performance of hybrid U-Joints – with a faster assembling cycle than traditional DA techniques [15,23,26]. Nevertheless, the ULSF and DaB reached in this study are superior to those reported in a previous study in which the combination of additively manufactured 316L and unreinforced PEEK hybrid joints were explored [15]. This improvement can be associated with the addition of carbon fibers, which increases the strength and modulus of the polymeric material. On the other hand, Feistauer [22] explored the joinability of MIM Ti-6Al-4 V and laminated glass-fiber reinforced PEI via U-Joining and reached a similar ULSF (3.6 ± 0.4 kN) but a way lower DaB (1.30 ± 0.08 mm). This difference can be associated with two factors: the much smoother surface roughness of the MIM parts, which strongly reduces the micromechanical interlocking between the parts, and the differences between the elongation at break for both metallic materials – around 20% for MIM Ti-6Al-4 V [22] and 50% for 316L SS [29]. The elongation at break has a strong influence on the observed fracture mechanism, as with the increased shear strain in a lap shear test, the yield limit is exceeded for the 316L SS and the TTRs start to
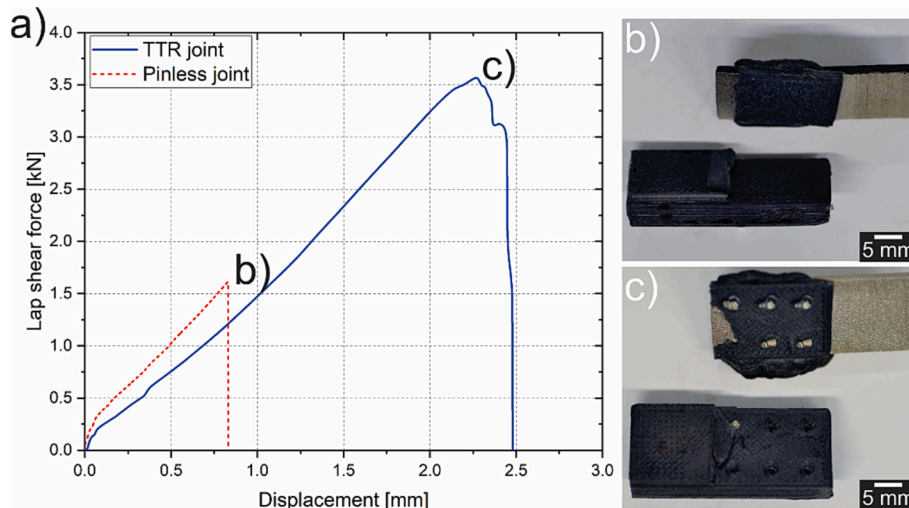

Fig. 16. A) representative force–displacement curves, comparing a pinless reference and a U-Joint; b) and c) a fractured pinless and a U-Joint, respectively.

plastically deform and lean in the direction of the applied load (as observed in Fig. 16-c). However, the Ti-6Al-4 V fails before any plastic deformation can be observed, and the crack propagates through the base of all the TTRs, which generates a subsequent failure mode between them [22]. It is important to highlight that these different fracture mechanisms increase the fracture toughness of joints under different loading conditions.

Fig. 16-c) also shows that the surface of the TTRs was partially exposed and, for a better understanding of the failure mechanisms, SEM analyses were conducted on the fractured surface and are presented in Fig. 17. The detailed SEM images (Fig. 17-b and -c) reveal that a significant portion of PEEK-20CF remained adherend to certain surface regions of the 316L SS connector even after testing, indicating a combination of localized adhesive and cohesive failure. The overview picture (Fig. 17-a) also suggests that the net tension caused the component to fail at the end of the overlap region. These results confirm the effective wetting of the 316L SS surface by the molten polymer, resulting in strong bonds between both materials. Additionally, Fig. 17-b) and -c) indicate that the rough surface produced by the LPBF process enhanced the micromechanical interlocking between the materials and the mechanical performance of the joint.

The microstructural analyses (Fig. 14) and microhardness mapping (Fig. 15) indicate that the 316L SS material was not strongly affected by the welding cycle, and this corroborates the idea that the U-Joining is a process with localized and controlled heat development. However, Fig. 3-c) indicates that the process leaves marks on the surface of the metallic part, which resemble the tool geometry, demonstrating that the tool mildly penetrates the material at its surface. Feistauer [22] noted that the tool needs to penetrate to effectively grip the metal part during joining and transfer the vibration of the sonotrode to the interface of the material, thereby preventing any slipping between the joint metallic part and the tool. In addition, Fig. 3-c) also shows that the region in contact with the tool was partially oxidized. Since this surface finishing and condition is a concern regarding the corrosion properties of joints, the corrosion resistance was evaluated at that region for as-built and joints produced with optimized and HEI (E_J of 8000 J) parameters. Fig. 18-a) shows the obtained potentiodynamic polarization curves and the identified corrosion potentials (E_{corr}) and pitting potential (E_{pit}) values are summarized in Table 6.

It can be seen that the E_{corr} values (Table 6) are similar for all the analyzed conditions during the polarization tests in the 3.5 wt% NaCl solution. This is also highlighted in Fig. 18-b) and indicates that the U-Joining process does not induce changes in the rates of anodic and cathodic reactions while the material corrodes spontaneously.

The polarization curves revealed distinctive shapes for the anodic regions, characterized by a zone of stable current density followed by a rapid increase in current density, which are typical aspects of the passive and passive film breakdown behavior, respectively. The as-built material exhibits superior pitting corrosion resistance compared to the joined samples (which is indicated by the higher E_{pit} values). Moreover, all the samples showed anodic current fluctuations (indicated by arrows in Fig. 18-c), which are related to metastable pitting. These results and the averaged E_{pit} values indicate that the joining cycle reduced the corrosion resistance for both joined conditions, with the optimized one having a

higher localized corrosion resistance than the HEI (as $E_{pit,opt} > E_{pit,HEI}$).

Qiu et al. [60] showed that LPBF 316L SS parts present, in general, good chemical homogeneity down to the micron level. However, in the same study, nano-segregation and Mn-Si-O enriched precipitates homogeneously distributed throughout the samples could be observed. The same results were reported by Deng et al. [61] and Ura-Bińczyk et al. [62], which explored the influence of different heating cycles on these precipitates. According to their findings, high temperatures are responsible for coarsening these nano-inclusions, increasing their size and reducing their numbers. Ura-Bińczyk et al. [62] showed that as-built 316L SS containing nano-inclusions with an average size of 26 nm displayed improved localized corrosion resistance, whereas the corrosion resistance of heat-treated samples, with an average nano-inclusion size of 52 nm, significantly decreased, even though there was no significant difference in their chemical composition. This outcome suggested that the pitting corrosion is triggered by a critical size of the nano-inclusions, which depends on the heating cycle applied to the material. The reported behavior is in accordance with what was observed in the present study. As shown and discussed in Fig. 13, the temperatures reached by the U-Joining process depend on the joining parameters, meaning that HEI samples undergo a higher heating cycle, which should result in coarser precipitates and reduces the observed localized corrosion resistance. This assumption would confirm the changes in the corrosion behavior and the fact that variations were not observed in the microhardness profiles (Fig. 15). However, further detailed microstructural studies, which are out of the scope of this study – regarding the influence of the joining cycle on the material's nanostructure are needed to further confirm these assumptions.

Additionally, Zhao et al. [63] observed that the pitting corrosion in AM 316L SS is developed by initiating pitting in new locations and their expansion. The author described the interrelated dynamic process involving the formation and damage of the oxide film on the surface, which is also evident in the fluctuations depicted in Fig. 18-c). The regeneration of the damaged oxide film plays a crucial role in preventing the cavities from progressing into pits. However, if one cavity transforms into a pit, it can impede the development of other cavities into pits due to the formation of a corrosion couple. In addition, nearby pits may combine to form a single large pit during growth. As a result, despite the formation of numerous cavities during corrosion tests at the initial stage, only a few pits are ultimately formed. Fig. 19 shows the corrosion morphology analyses obtained via SEM of the largest pits identified at the 316L SS surface after potentiodynamic polarization tests.

The images show that the identified pits have an elongated morphology, which could be associated with the merging of micro-pits as described in the literature [63]. This phenomenon reveals a typical way for pit expansion for all the conditions, i.e., larger pits continuously swallowing the smaller ones. The optimized condition showed a higher density of micro-pit (Fig. 19-b) than the as-built (Fig. 19-a), which could be associated with the nanoprecipitates growth. On the other hand, the HEI shows a lower concentration of micro-pits, but a deeper corrosion pit, which indicates a change in the corrosion mechanism. As explained by Ura-Bińczyk et al. [62], the larger the precipitates, the greater the intensity of the galvanic cell formed between them and the matrix, and the more intense the corrosion. This could mean that the size reached by
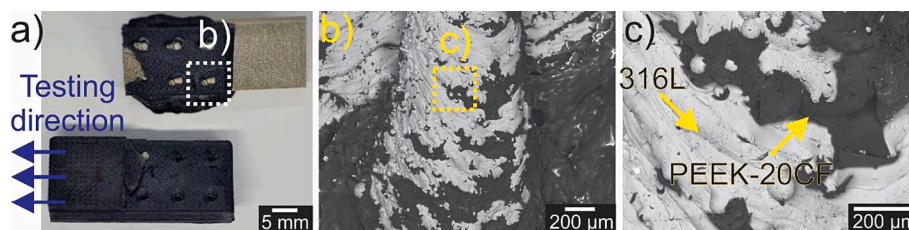

Fig. 17. A) overview of a fractured sample after a quasi-static lap shear test, exposing the metal-polymer interface; b) and c) show detailed sem views of the fracture surface.
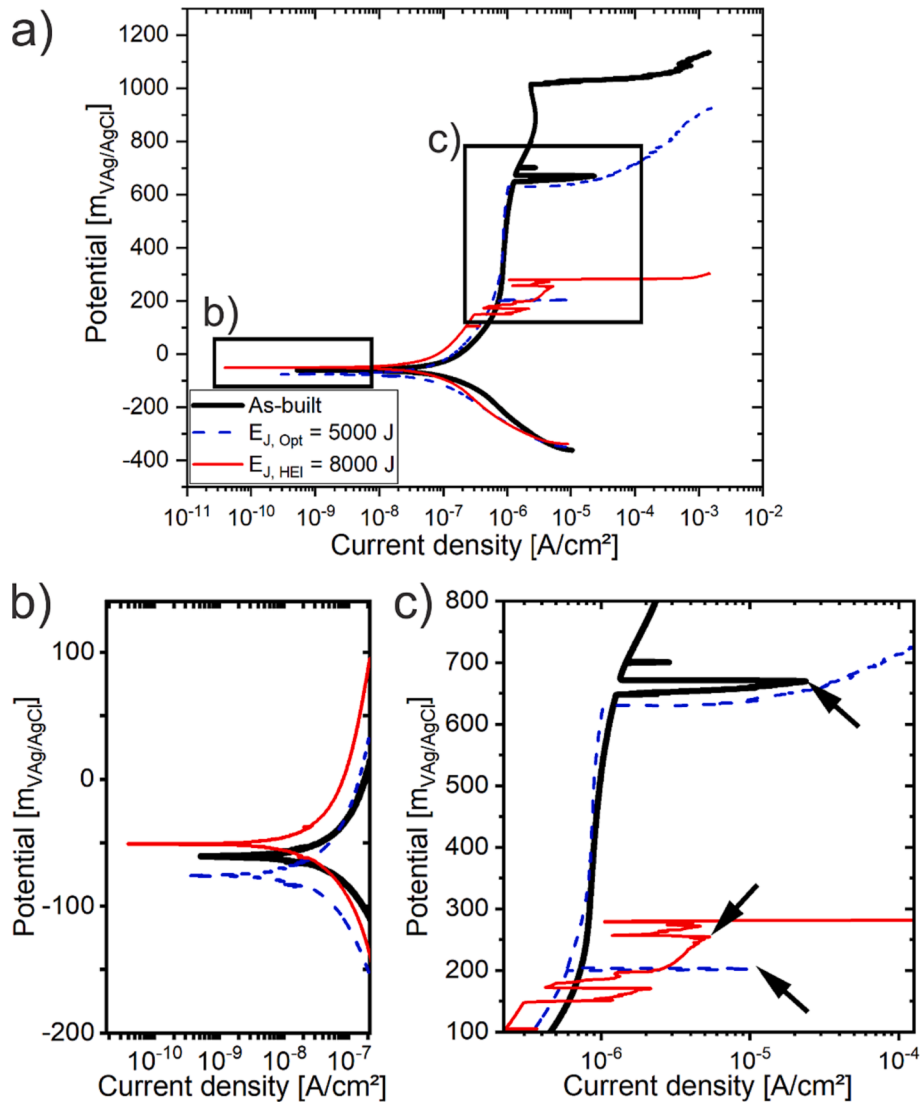
Fig. 18. A) potentiodynamic polarization curves obtained in 3.5 wt% NaCl solution for the as-built, optimized and higher energy input conditions; b) and c) show detailed views of the marked regions.

Table 6
Electrochemical corrosion parameters obtained from potentiodynamic polarization curves in 3.5 wt% NaCl solution for the as-built 316L SS, as well as the 316L SS in the optimized and higher energy input U-Joining conditions.

Condition	E_{corr} (mV$_{Ag/AgCl}$)	E_{pit} (mV$_{Ag/AgCl}$)
As-built	-69 ± 9	1018 ± 56
Optimized	-90 ± 20	655 ± 25
Higher energy input	-61 ± 8	273 ± 15

the precipitates when using HEI induces intense pit corrosion (which would result in an increment in the depth of the pits formed), instead of micro-pits nucleation. The detailed view presented in (Fig. 19-c) corroborates this idea. In conclusion, although the potentiodynamic polarization tests indicated that the joining cycle negatively affects the local corrosion behavior of the additively manufactured 316L SS, the changes in the nanostructure for the optimized condition appear to not be sufficient to change the main corrosion mechanism. The same behavior was not observed for the HEI level hybrid joints, as deeper pits were identified; these suggest a change in corrosions mechanism. A deeper investigation of the corrosion kinetics is required to confirm this assumption. However, this is out of the scope of this manuscript.

4. Conclusions

This study investigated the ultrasonic joining (U-Joining) optimization and understanding for additively-manufactured (AM) 20% short-carbon-fiber reinforced PEEK (PEEK-20CF) and 316L stainless steel (316L SS) hybrid joints. Based on the obtained results, the following conclusions can be made:

- Wettability tests were performed at the surface of as-built 316L SS using PEEK-20CF filament to determine their interaction by analyzing their contact angle. The results show that the contact angle between both materials is generally higher than 100°, which can be explained by the low surface energy of the 316L SS and entrapped gases at the interface, preventing complete surface wetting and producing poor adhesion forces between both materials.
- The U-Joining process parameters were optimized via a Box-Behnken design of experiments to ensure a proper surface wetting of the metallic surface and, consequently, the micromechanical interlocking and chemical bonds between the metal and the composite. The study aimed to maximize the achieved ultimate lap shear force (ULSF) response and resulted in the optimized set of parameters: joining energy (E_J) of 5000 J, sonotrode amplitude (A_O) of 120 μm
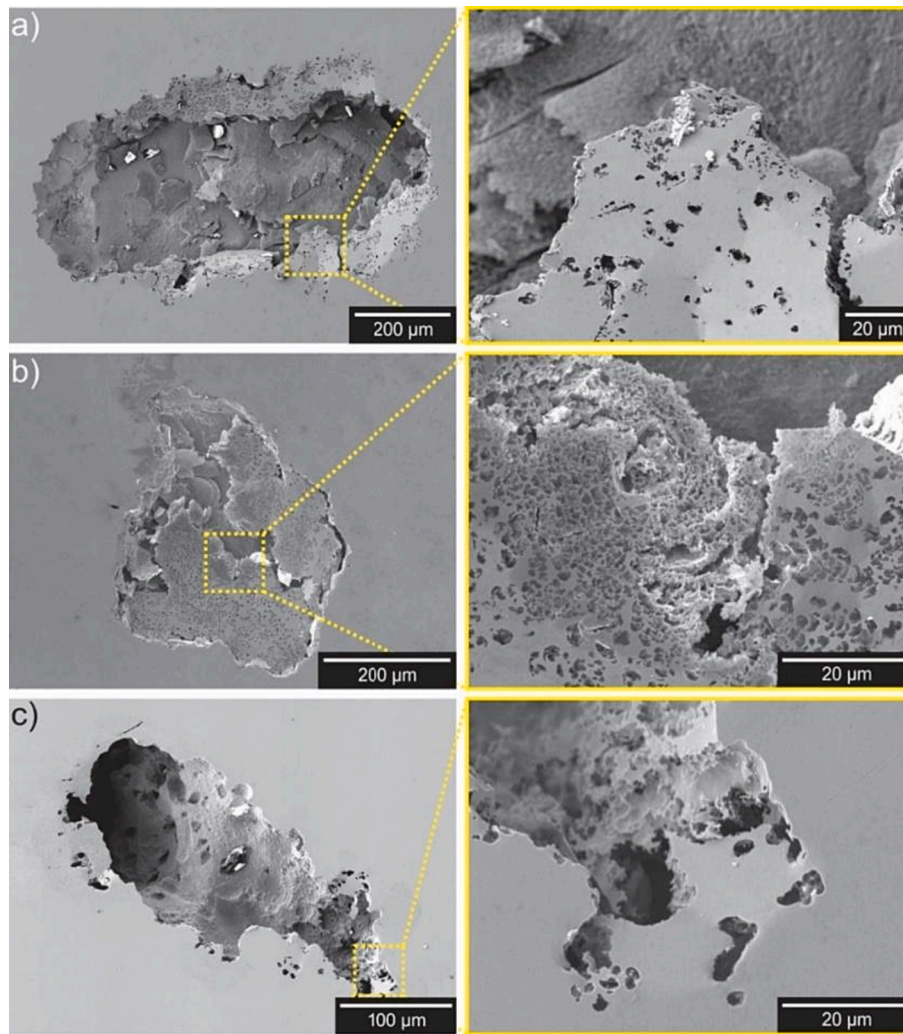
Fig. 19. Morphological characteristics of pitting corrosion on the surface of 316L SS samples after potentiodynamic polarization in 3.5 wt% NaCl solution for a) as-built, b) optimized and c) HEI joined conditions.

and joining pressure (J_P) of 60 psi, produced joints with an average ULSF of 3.6 ± 0.3 kN and reached a joining time of approximately 3 s.

- A systematic and stepwise stop-action study was conducted to understand the joint formation using the optimized parameters, but with incremental E_J. The results showed that strong joints are formed only at very high energy inputs for rough AM 316L SS and that the E_J necessary for that purpose can be twice as high as the levels needed for smooth metallic connectors.
- The process temperature development along the optimized joining cycle was monitored, indicating that the desired 316L SS surface wetting by molten PEEK-20CF was achieved. Additional microstructural analyses showed strong micromechanical interlocking between the consolidated PEEK-20CF and the 316L SS surface, whereby the filling of crevices at the metallic connector's rough surface took place. This strong interlocking resulted in a mixture of adhesive, cohesive, and net tension failures during the quasi-static mechanical tests.
- Potentiodynamic polarization tests at the joined surface showed that the joining cycle reduced the pitting corrosion resistance of the hybrid joints compared to as-built 316L SS specimens, and that the higher the energy input, the stronger the reduction, making it more susceptible to localized corrosion. This decrease was associated with the coarsening of nano-segregations at the base material. Additional pitting corrosion morphology analyses showed pit growth as the

primary localized corrosion mechanism observed for all U-joining conditions.

CRediT authorship contribution statement

Willian S. de Carvalho: Writing – review & editing, Writing – original draft, Methodology, Investigation, Formal analysis, Conceptualization. **Guilherme S. Vacchi:** Writing – review & editing, Methodology, Investigation, Formal analysis, Conceptualization. **Carlos A.D. Rovere:** Writing – review & editing, Supervision, Supervision, Funding acquisition, Formal analysis. **Sergio T. Amancio-Filho:** Writing – review & editing, Supervision, Funding acquisition, Formal analysis, Conceptualization.

Declaration of Competing Interest

The authors declare that they have no known competing financial interests or personal relationships that could have appeared to influence the work reported in this paper.

Data availability

Data will be made available on request.

Acknowledgments

References

[1] European commission (EC), "Updated analysis of the non-CO2 effects of aviation," Nov. 24, 2020. https://ec.europa.eu/clima/news-your-voice/news/updated-analysis-non-co2-effects-aviation-2020-11-24_en (accessed Oct. 28, 2022).

[2] X. Cui, H. Zhang, S. Wang, L. Zhang, J. Ko, Design of lightweight multi-material automotive bodies using new material performance indices of thin-walled beams for the material selection with crashworthiness consideration, Materials and Design 32 (2) (Feb. 2011) 815–821, https://doi.org/10.1016/J.MATDES.2010.07.018.

[3] K. Ramaswamy, R.M. O'Higgins, M.C. Corbett, M.A. McCarthy, C.T. McCarthy, Quasi-static and dynamic performance of novel interlocked hybrid metal-composite joints, Composite Structures 253 (Dec. 2020), 112769, https://doi.org/10.1016/J.COMPSTRUCT.2020.112769.

[4] G. Marsh, Airbus takes on boeing with reinforced plastic A350 XWB, Reinforced Plastics 51 (11) (Dec. 2007) 26–29, https://doi.org/10.1016/S0034-3617(07)70383-1.

[5] G. Marsh, Bombardier throws down the gauntlet with CSeries airliner, Reinforced Plastics 55 (6) (Nov. 2011) 22–26, https://doi.org/10.1016/S0034-3617(11)70181-3.

[6] F. Faupel, R. Willecke, A. Thran, Diffusion of metals in polymers, Mater. Sci. Eng. R Reports 22 (1) (Mar. 1998) 1–55, https://doi.org/10.1016/S0927-796X(97)00020-X.

[7] K. Bodjona, S. Fielding, M. Heidari-Rarani, L. Lessard, Effect of adhesive layer compliance on strength of single-lap hybrid bonded-bolted joints, Composite Structures 261 (Apr. 2021), 113324, https://doi.org/10.1016/J.COMPSTRUCT.2020.113324.

[8] B. C. P. Jongbloed, J. J. E. Teuwen, R. Benedictus, and I. F. Villegas, "A Study on Through-the-Thickness Heating in Continuous Ultrasonic Welding of Thermoplastic Composites," *Mater. 2021, Vol. 14, Page 6620*, vol. 14, no. 21, p. 6620, Nov. 2021, doi: 10.3390/MA14216620.

[9] S.M. Doshi, T.B. Lyness, E.T. Thostenson, Damage monitoring of adhesively bonded composite-metal hybrid joints using carbon nanotube-based sensing layer, Nanocomposites 6 (1) (2020) 12–21.

[10] R. W. Messler, "Joining of Materials and Structures: From Pragmatic Process to Enabling Technology," *Join. Mater. Struct. From Pragmatic Process to Enabling Technol.*, pp. 1–790, 2004, doi: 10.1016/B978-0-7506-7757-8.X5000-3.

[11] S.T. Amancio-Filho, L.A. Blaga, Joining of polymer-metal hybrid structures: Principles and applications, Join. Polym. Hybrid Struct. Princ. Appl. (Jan. 2018) 1–394, https://doi.org/10.1002/9781119429807.

[12] W. S. de Carvalho, M. C. Vioreanu, M. R. A. Lutz, G. P. Cipriano, and S. T. Amancio-Filho, "The Influence of Tool Wear on the Mechanical Performance of AA6061-T6 Refill Friction Stir Spot Welds," *Mater. 2021, Vol. 14, Page 7252*, vol. 14, no. 23, p. 7252, Nov. 2021, doi: 10.3390/MA14237252.

[13] E. E. Feistauer, R. P. M. Guimarães, T. Ebel, J. F. Dos Santos, and S. T. Amancio-Filho, "Ultrasonic joining: A novel direct-assembly technique for metal-composite hybrid structures," *Mater. Lett.*, vol. 170, pp. 1–4, May 2016, doi: 10.1016/J.MATLET.2016.01.137.

[14] V. Di Giandomenico, "Surface structured bonded composite-metal joint," *Ph.D. Diss. Cranf. Univ. 2014*, Accessed: Oct. 28, 2022. [Online]. Available: https://dspace.lib.cranfield.ac.uk/handle/1826/9308.

[15] W.S. de Carvalho, S.T. Amancio-Filho, On the feasibility of joining additively-manufactured 316L stainless steel and poly-ether-ether-ketone by ultrasonic energy, Addit. Manuf. Lett. 3 (Dec. 2022), 100098, https://doi.org/10.1016/J.ADDLET.2022.100098.

[16] R. Oluleke, "Metallurgical Performance of Hyper - Joints In Composite to Metal Joining," *Ph.D. Diss. Univ. Manchester, 2015*, Accessed: Oct. 28, 2022. [Online]. Available: https://www.research.manchester.ac.uk/portal/en/theses/metallurgical-performance-of-hyper–joints-in-composite-to-metal-joining(6a87e957-d6f1-4d78-b989-a68dc39d41cf).html.

[17] C. Earl, J.R. Castrejón-Pita, P.A. Hilton, W. O'Neill, The dynamics of laser surface modification, Journal of Manufacturing Processes 21 (Jan. 2016) 214–223, https://doi.org/10.1016/J.JMAPRO.2015.10.002.

[18] S. Ucsnik, M. Scheerer, S. Zaremba, D.H. Pahr, Experimental investigation of a novel hybrid metal–composite joining technology, Composites. Part A, Applied Science and Manufacturing 41 (3) (Mar. 2010) 369–374, https://doi.org/10.1016/J.COMPOSITESA.2009.11.003.

[19] P.N. Parkes, R. Butler, J. Meyer, A. de Oliveira, Static strength of metal-composite joints with penetrative reinforcement, Composite Structures 118 (1) (Dec. 2014) 250–256, https://doi.org/10.1016/J.COMPSTRUCT.2014.07.019.

[20] F. Smith, Comeld™: an innovation in composite to metal joining, Materials and Technologies 20 (2) (2016) 91–96, https://doi.org/10.1080/10667857.2005.11753117.

[21] S.A. Ucsnik, G. Kirov, New possibility for the connection of metal sheets and fiber reinforced plastics, Materials Science Forum 690 (2011) 465–468, https://doi.org/10.4028/WWW.SCIENTIFIC.NET/MSF.690.465.

[22] E. E. Feistauer, "Ultrasonic joining of through-the-thickness reinforced metal-composite hybrid structures," *Ph.D. Diss. Tech. Univ. Hamburg, 2019*, doi: 10.15480/882.1956.

[23] W. S. de Carvalho and S. T. Amancio-Filho, "Ultrasonic joining of additively manufactured metal-polymer lightweight hybrid structures," in *Annual Technical Conference - ANTEC, Conference Proceedings*, vol. 1, p. 526.

[24] W. S. De Carvalho, N. F. Colvin, A. Benatar, and S. T. Amancio-Filho, "Ultrasonic Joining of Additively Manufactured Metal-Composite Hybrid Joints: A Comparison between Vertical and Horizontal Vibration Modes," *Met. 2023, Vol. 13, Page 319*, vol. 13, no. 2, p. 319, Feb. 2023, doi: 10.3390/MET13020319.

[25] I.F. Villegas, H.E.N. Bersee, Ultrasonic welding of advanced thermoplastic composites: An investigation on energy-directing surfaces, Advances in Polymer Technology 29 (2) (Jun. 2010) 112–121, https://doi.org/10.1002/ADV.20178.

[26] E.E. Feistauer, J.F. dos Santos, S.T. Amancio-Filho, An investigation of the ultrasonic joining process parameters effect on the mechanical properties of metal-composite hybrid joints, Weld. World 64 (9) (Sep. 2020) 1481–1495, https://doi.org/10.1007/S40194-020-00927-X/FIGURES/15.

[27] N. Sarantinos, V. Kostopoulos, G. Di Vita, G. Campoli, L. Bricout, Micro-pins: the next step in composite–composite and metal–composite joining, CEAS Space J 11 (3) (2019) 351–358.

[28] H. Roirand, B. Malard, A. Hor, N. Saintier, Effect of laser scan pattern in laser powder bed fusion process: the case of 316L stainless steel, Procedia Struct. Integr. vol. 38, no. C (Jan. 2022) 149–158, https://doi.org/10.1016/J.PROSTR.2022.03.016.

[29] S.D. Washko, G. Aggen, Wrought Stainless Steels, Properties and Selection: Irons, Steels, and High-Performance Alloys Vol 1 (1990) 841–907.

[30] W.S. de Carvalho, J. Draper, T. Terrazas-Monje, A. Toumpis, A. Galloway, S. T. Amancio-Filho, Fatigue life assessment and fracture mechanisms of additively manufactured metal-fiber reinforced thermoplastic hybrid structures produced via ultrasonic joining, Journal of Materials Research and Technology 26 (2023) 5716–5730.

[31] "ASTM B962-15 Standard Test Methods for Density of Compacted or Sintered Powder Metallurgy (PM) Products Using Archimedes' Principle, American Society for Testing and Materials, Pennsylvania, United States." https://www.astm.org/b0962-15.html (accessed Nov. 30, 2022).

[32] W.S. de Carvalho, F. Marzemin, C. Belei, S. Petersmann, F. Arbeiter, S.T. Amancio-Filho, Statistical-based optimization of fused filament fabrication parameters for short-carbon-fiber-reinforced poly-ether-ether-ketone considering multiple loading conditions, Polymer Testing 128 (2023) 108207.

[33] "PEEK+CF20 Professional Carbon Fiber 3D Printing Filament." https://www.3dxtech.com/product/carbonx-peek-cf20/ (accessed Mar. 19, 2023).

[34] R.H. Myers, D.C. Montgomery, C.M. Anderson-Cook, *Response surface methodology: Process and product optimization using designed experiments*, 4th editio, Wiley, 2016.

[35] "ASTM E384-11 Standard Test Method for Knoop and Vickers Hardness of Materials, American Society for Testing and Materials, Pennsylvania, United States" doi: 10.1520/E0384-11.

[36] "ASTM G5-94 Standard Reference Test Method for Making Potentiostatic and Potentiodynamic Anodic Polarization Measurements, American Society for Testing and Materials, Pennsylvania, United States" Accessed: Nov. 30, 2022. [Online]. Available: https://www.astm.org/g0005-94r11e01.html.

[37] M.E. Kazemi, L. Shanmugam, L. Yang, J. Yang, A review on the hybrid titanium composite laminates (HTCLs) with focuses on surface treatments, fabrications, and mechanical properties, Composites. Part A, Applied Science and Manufacturing 128 (Jan. 2020), 105679, https://doi.org/10.1016/J.COMPOSITESA.2019.105679.

[38] R.G.J. Van Rooijen, J. Sinke, S. Van Der Zwaag, Improving the adhesion of thin stainless steel sheets for fibre metal laminate (FML) applications, Journal of Adhesion Science and Technology 19 (16) (2012) 1387–1396, https://doi.org/10.1163/156856105774805840.

[39] H.C. Man, D.R. Gabe, The determination of pitting potentials, Corrosion Science 21 (4) (Jan. 1981) 323–326, https://doi.org/10.1016/0010-938X(81)90007-X.

[40] D. Thomas, The development of design rules for selective laser melting, Ph.D. Diss. Cardiff Metrop. Univ. (2009, Oct. 2009,), https://doi.org/10.25401/CARDIFFMET.20974597.V1.

[41] G. Piscopo, A. Salmi, E. Atzeni, On the quality of unsupported overhangs produced by laser powder bed fusion, International Journal of Manufacturing Research 14 (2) (2019) 198–216, https://doi.org/10.1504/IJMR.2019.100012.

[42] D. Wang, Y. Yang, R. Liu, D. Xiao, J. Sun, Study on the designing rules and processability of porous structure based on selective laser melting (SLM), Journal of Materials Processing Technology 213 (10) (Oct. 2013) 1734–1742, https://doi.org/10.1016/J.JMATPROTEC.2013.05.001.

[43] F. Calignano, investigation of the accuracy and roughness in the laser powder bed fusion process, Virtual Phys. Prototyp. 13 (2) (Apr. 2018) 97–104, https://doi.org/10.1080/17452759.2018.1426368.

[44] D.J.C. Gomes, N.C. De Souza, J.R. Silva, Using a monocular optical microscope to assemble a wetting contact angle analyser, Measurement 46 (9) (Nov. 2013) 3623–3627, https://doi.org/10.1016/J.MEASUREMENT.2013.07.010.

[45] G. Zhang, Q. Zhu, H. Yang, C. Yang, Y. Liu, C. Wang, Effect of surface treatments on the laser welding performance of dissimilar materials, Journal of Manufacturing Processes 74 (Feb. 2022) 465–473, https://doi.org/10.1016/J.JMAPRO.2021.12.044.

[46] N. Manente André, S.M. Goushegir, N. Scharnagl, J.F. dos Santos, L.B. Canto, S.T. Amancio-Filho, Composite surface pre-treatments: Improvement on adhesion mechanisms and mechanical performance of metal–composite friction spot joints with additional film interlayer, The Journal of Adhesion 94 (9) (2018) 723–742.

[47] A. Benatar, Plastics joining, Appl. Plast. Eng. Handb. Process. Mater. Appl. Second Ed. (Jan. 2017) 575–591, https://doi.org/10.1016/B978-0-323-39040-8.00027-4.

[48] H. Potente, *Fügen von Kunststoffen Grundlagen, Verfahren, Anwendung*. Hanser, 2004, 2004. Accessed: Nov. 27, 2022. [Online]. Available: https://books.google.com/books/about/Fügen_von_Kunststoffen.html?id=J9K5wAEACAAJ.

[49] V.K. Stokes, Analysis of the friction (spin)-welding process for thermoplastics, Journal of Materials Science 23 (8) (1988) 2772–2785.

[50] M.N. Tolunay, P.R. Dawson, K.K. Wang, Heating and bonding mechanisms in ultrasonic welding of thermoplastics, Polymer Engineering and Science 23 (13) (Sep. 1983) 726–733, https://doi.org/10.1002/PEN.760231307.

[51] M. Biron, thermoplastics and thermoplastic composites: Technical information for plastics users, Thermoplast. Thermoplast. Compos. Tech. Inf. Plast. Users (Aug. 2007) 1–874, https://doi.org/10.1016/B978-1-85617-478-7.X5001-6.

[52] G.P. Cipriano, W.S. de Carvalho, P. Vilaça, S.T. Amancio-Filho, thermomechanical modeling of the metallic rivet in friction riveting of amorphous thermoplastics, Weld. World 65 (5) (May 2021) 855–864, https://doi.org/10.1007/S40194-020-01049-0/FIGURES/7.

[53] A.B. Abibe, M. Sônego, J.F. dos Santos, L.B. Canto, S.T. Amancio-Filho, On the feasibility of a friction-based staking joining method for polymer–metal hybrid structures, Materials and Design 92 (Feb. 2016) 632–642, https://doi.org/10.1016/J.MATDES.2015.12.087.

[54] F. Staab, F. Balle, Ultrasonic torsion welding of ageing-resistant Al/CFRP joints: Properties, microstructure and joint formation, Ultrasonics 93 (Mar. 2019) 139–144, https://doi.org/10.1016/J.ULTRAS.2018.11.006.

[55] S. Singh, C. Prakash, S. Ramakrishna, 3D printing of polyether-ether-ketone for biomedical applications, European Polymer Journal 114 (May 2019) 234–248, https://doi.org/10.1016/J.EURPOLYMJ.2019.02.035.

[56] P. Patel, T.R. Hull, R.W. McCabe, D. Flath, J. Grasmeder, M. Percy, Mechanism of thermal decomposition of poly(ether ether ketone) (PEEK) from a review of decomposition studies, Polymer Degradation and Stability 95 (5) (May 2010) 709–718, https://doi.org/10.1016/J.POLYMDEGRADSTAB.2010.01.024.

[57] K.W. Jung, Y. Kawahito, M. Takahashi, S. Katayama, Laser direct joining of carbon fiber reinforced plastic to zinc-coated steel, Materials and Design 47 (May 2013) 179–188, https://doi.org/10.1016/J.MATDES.2012.12.015.

[58] S. Riehm, V. Friederici, S. Wieland, Y. Deng, S. Herzog, A. Kaletsch, C. Broeckmann, Tailor-made functional composite components using additive manufacturing and hot isostatic pressing, Powder Metallurgy 64 (4) (2021) 295–307.

[59] N. van de Werken, P. Koirala, J. Ghorbani, D. Doyle, M. Tehrani, Investigating the hot isostatic pressing of an additively manufactured continuous carbon fiber reinforced PEEK composite, Additive Manufacturing 37 (Jan. 2021), 101634, https://doi.org/10.1016/J.ADDMA.2020.101634.

[60] C. Qiu, M. Al Kindi, A. S. Aladawi, and I. Al Hatmi, "A comprehensive study on microstructure and tensile behaviour of a selectively laser melted stainless steel," *Sci. Reports 2018 81*, vol. 8, no. 1, pp. 1–16, May 2018, doi: 10.1038/s41598-018-26136-7.

[61] P. Deng, M. Karadge, R.B. Rebak, V.K. Gupta, B.C. Prorok, X. Lou, Evolution and impact of oxygen inclusions in 316L stainless steel manufactured by laser powder bed fusion, Conf. Proc. Soc. Exp. Mech. Ser. 7 (2021) 81–86, https://doi.org/10.1007/978-3-030-59864-8_13/FIGURES/4.

[62] E. Ura-Bińczyk, A. Dobkowska, P. Bazarnik, J. Ciftci, A. Krawczyńska, W. Chromiński, T. Wejrzanowski, R. Molak, R. Sitek, T. Płociński, J. Jaroszewicz, J. Mizera, Effect of annealing on the mechanical and corrosion properties of 316L stainless steel manufactured by laser powder bed fusion, Materials Science and Engineering A 860 (2022) 144263.

[63] C. Zhao, Y. Bai, Y. Zhang, X. Wang, J.M. Xue, H. Wang, Influence of scanning strategy and building direction on microstructure and corrosion behaviour of selective laser melted 316L stainless steel, Materials and Design 209 (Nov. 2021), 109999, https://doi.org/10.1016/J.MATDES.2021.109999.